

**MOLECULAR DYNAMICS
SIMULATIONS STUDY OF [5]ROTAXANE
IN BULK AND AT INTERFACES**

A THESIS SUBMITTED TO
THE GRADUATE SCHOOL OF ENGINEERING AND SCIENCE
OF BILKENT UNIVERSITY
IN PARTIAL FULFILLMENT OF THE REQUIREMENTS FOR
THE DEGREE OF
MASTER OF SCIENCE
IN
MATERIALS SCIENCE AND NANOTECHNOLOGY

By
Ata Utku Özkan
June 2022

July 17, 2022

Molecular Dynamics Simulations study of [5]Rotaxane in bulk and
at interfaces

By Ata Utku ÖZKAN

June 2022

We certify that we have read this thesis and that in our opinion it is fully adequate, in scope and in quality, as a thesis for the degree of Master of Science.

Aykur Erbaş (Advisor)

Dönüş Tuncel

Uğur Bozkaya

Approved for the Graduate School of Engineering and Science:

 Ezhan Kardeş
Director of the Graduate School

Declaration of Authorship

I, Ata Utku ÖZKAN, declare that this thesis titled, “Molecular Dynamics Simulations study of [5]Rotaxane in bulk and at interfaces” and the work presented in it are my own. I confirm that:

- This work was done wholly or mainly while in candidature for a research degree at this University.
- Where any part of this thesis has previously been submitted for a degree or any other qualification at this University or any other institution, this has been clearly stated.
- Where I have consulted the published work of others, this is always clearly attributed.
- Where I have quoted from the work of others, the source is always given. With the exception of such quotations, this thesis is entirely my own work.
- I have acknowledged all main sources of help.
- Where the thesis is based on work done by myself jointly with others, I have made clear exactly what was done by others and what I have contributed myself.

Signed:

Date:

“To achieve great things, two things are needed; a plan, and not quite enough time.”

Leonard Bernstein

BILKENT UNIVERSITY

Abstract

National Nanotechnology Research Center - UNAM

Master of Science

Molecular Dynamics Simulations study of [5]Rotaxane in bulk and at interfaces

by Ata Utku ÖZKAN

Rotaxanes are a class mechanically interlocked molecular architectures that exhibit quasi-mechanical movement in response to specific stimuli. [5]Rotaxane is a complex rotaxane structure that is reported to show extraordinary cytotoxic properties with light stimuli. By using all-atom classical molecular dynamics simulations, we study equilibrium and kinetics properties of various charge states of [5]rotaxane in salt-free water as well as [5]Rotaxane network derivatives at the interface of water and chloroform. By analyzing molecular configurations, hydrogen bonding and size, energy based metrics of individual molecules both in bulk and water-chloroform interfaces, we demonstrate that charge-state of [5]rotaxane directly influences the molecular conformation and solvation properties. While charge-neutral and negatively charged molecules often tend to collapse in a way that they expose their porphyrin core, positively charged moieties tend to take more extended molecular configuration screening the core. Further, sudden changes in the charge states emulating the pH alterations in solution conditions leads to gradual, 1000-ps level, changes in molecular conformation of [5]rotaxane via shuttling motion of CB6 rings along [5]rotaxane axles. Finally, simulations with 2D networks of [5]rotaxane confirm the possibility of molecular film formation at hydrophobic-hydrophilic interfaces. Overall, our results suggest that [5]rotaxane can exhibit a rich spectrum of molecular configurations and assembly properties depending on the ionic strengths of the solution or external stimuli.

Keywords: Molecular Dynamics, [5]Rotaxane, CB6, Molecular Switch

ÖZET

Ulusal Nanoteknoloji Araştırma Merkezi - UNAM

[5]Rotaxane molekülünün Toplu Halde ve Arayüzlerdeki Moleküler Dinamik Simülasyonları

Ata Utku Özkan

Malzeme Bilimi ve Nanoteknoloji, Yüksek Lisans

Rotaxaneler, mekanik olarak birbirine kenetlenmiş moleküllerin bir alt sınıfıdır. Belirli çevresel uyarılara tepki olarak yarı-mekanik, kimyasal olmayan moleküler hareket sergilerler. [5]Rotaxane, yapısı nedeniyle beklenmedik kimyasal ve mekanik özellikler gösteren karmaşık bir rotaxen yapısıdır. [5]Rotaxane sistemine ışık uygulandığında hücre öldürücü özellik sergiler. Bu çalışmada atomistik klasik moleküler dinamik simülasyonları kullanılarak [5]Rotaxane'in farklı yük durumlarındaki denge ve kinetik özellikleri tuzsuz suda, [5]Rotaxane network türevleri ise su ve kloroform arayüzünde simüle edilmiştir. Görsel moleküler konfigürasyon analizi, hidrojen bağı hesapları ve enerji bazlı metrikler kullanılarak hem toplu hem de su-kloroform arayüzlerinde, yük durumunun [5]Rotaxane'in yapısını tamamen değiştirdiği gösterilmiştir. Nötr ve negatif yüklü sistem aktif olarak porphyrin merkezini açığa çıkaracak şekilde çökme eğilimindeyken, pozitif yüklü sistem daha yayılmış düzlemsel bir konformasyon alma eğilimindedir. Ayrıca, çözelti koşullarındaki ani pH değişikliklerini taklit eden şarj durumları değişiklikleri, [5]Rotaxane in eksenlerindeki CB6 halkalarının kademeli olarak, ortalama 1000 ps hızla, kayma hareketi yapmasına sebep olmaktadır. Son olarak, yapılan simülasyonlar deneylerde gösterilen [5]rotaxane molekülünün hidrofobik-hidrofilik arayüzlerde film oluşturulabilme özelliğiyle örtüşür sonuçlar vermiştir. Sonuç olarak simülasyonlarımız, [5]Rotaxane molekülünün, zengin bir konformasyon spektrumuna sahip olduğunu ve çözeltinin iyonik durumuna ve ısı gibi dış etkilere bağlı olarak öztoplanma özelliğine sahip olduğunu göstermektedir.

Anahtar kelimeler: Moleküler Dinamik, [5]Rotaxane, CB6, Moleküler Şalter

Acknowledgements

I would like to express my most sincere gratitude to my supervisor Aykut Erbaş for his kind support, guidance and openness to discussion of my not so well articulated research ideas. I could not have imagined having a better advisor and mentor for my Master's study.

Besides my advisor, I would like to thank Dönüş Tuncel for her total guidance in my research project and physically synthesizing the molecule that is the focus of this thesis.

I am indebted to all members of Aykut Erbaş Research Group for their invaluable scientific and emotional support and the computational researchers of UNAM, Seymur Jahangirov and Engin Durgun for their very generous teaching and adviserships on the intricacies of atomistic systems.

Above all, I thank my family and soon to be my wife girlfriend for supporting me in all aspects of life and pushing me towards the success that I've never ever dreamed of.

Finally thanks to UNAM for providing the perfect research environment and extensive tools. I'm grateful to the institute for funding my research and I hope it will serve their interests well.

Contents

Declaration of Authorship	iv
Abstract	vi
Acknowledgements	viii
1 Introduction	1
1.0.1 Complex Rotaxanes	3
2 Basic Concepts	7
2.1 Theory	7
2.1.1 Classical Systems	7
2.1.2 Micro to Macro	11
2.2 Molecular Dynamics	13
2.2.1 Methodology	13
2.2.2 Forcefield	15
2.2.3 Analysis	17
3 Molecular Dynamics Simulations of [5]Rotaxane	21
3.1 Simulation Details, Results and Discussion	21
3.1.1 Charge Assignment	23
3.1.2 Configuration of single [5]Rotaxane	24
3.1.3 Effect of Charged Porphyrin Core on the Structure	31
3.2 Kinetics Studies of [5]Rotaxane Shuttling	34
3.2.1 POS \leftrightarrow POS-R	34
3.2.2 POS \leftrightarrow NEUT-P	36
3.2.3 Essential Dynamics Analysis	38
3.3 Poly Rotaxane and Poly-[5]Rotaxane Network	43
3.3.1 PR Simulations	43
3.3.2 PN Simulations	45
4 Conclusion	49

A Essential Dynamics Figures	51
A.1 NEUT - Restrained	51
A.2 POS-R1	52
B Cumbersome Details of Simulations	54
Bibliography	56

List of Figures

1.1	The basic shape of simplest 2-rotaxane with decoupling preventing groups orange. Green rectangle shows the stable site for the macrocycle.	2
1.2	Switch-rot Representation	3
1.3	5-Rotaxane Structure and Sythesis	4
1.4	Polyrotaxane and Polyrotaxane Network	5
2.1	Bonded Interactions	8
2.2	Update Algorithm	17
2.3	Solvent Accesible Surface Area	18
2.4	Electronegative nitrogen groups hydrogen bonding with water atoms are shown as dashed blue lines, oxygen groups are shown as dashed red lines(bottom-left).	19
3.1	Charge States	22
3.2	Final conformations of different Rotaxane charge states. The protonation increases from top to bottom. First and last neg and pos-r2 states are the exotic states that are unlikely to be obtained experimentally.	24
3.3	Radius of gyration of charge states averaged over time and replicas	25
3.4	Drastic conformational change between non charged(neg) and positively charged(pos) states.	26
3.5	CB6 and corresponding axle Triazole distances of each charge state averaged over time and replicas.	27
3.6	Solvent accessible surface area of different charge states averaged over time and replicas.	28
3.7	Hydrogen Bonding of different charge states averaged over time and replicas. The adjacent dashed bars correspond to water - CB6 contribution.	29
3.8	Hydrogen Bonding Distance distribution of different charge states averaged over time and replicas, normalized.	30

3.9	Hydrogen Bonding Distance distribution of different charge states averaged over time and replicas, normalized.	31
3.10	Final structures of 10ns simulations. Central proton removed pos state is labeled as pos-c conformation(right).	32
3.11	Avegared RoG and SASA values of central proton removed pos-c state compared to pos state.	32
3.12	CB6 transition along axle in pos \leftrightarrow pos-r1 state change simulations. 2 of 4 rings randomly shuttle outwards along the axle with forward(purple) direction, only one of the shuttled CB6 shuttle back for backward(red) direction.	34
3.13	Solvent accessible surface area versus time data of both ways of transition(pos \leftrightarrow pos-r1). Red line denotes pos-r1 \rightarrow pos transition, purple line denotes pos \rightarrow pos-r1 transition.	35
3.14	Final equilibrium conformation of pos \rightarrow neut-p transition obtained after 5ns and neut state.	36
3.15	Final equilibrium conformation of pos \rightarrow neut-p transition obtained after 5ns and neut state.	37
3.16	High eigenvector trajectory of CB6 rings of pos-r1 state. Colored from starting time frame, red dots to final time frame blue dots denote average positions of CB6 atoms. Blue and Red circles are on the center of high density red and blue points.	39
3.17	Low eigenvector trajectory of CB6 rings of pos-r1 state. Colored from starting time frame positions(red dots) to final time frame positions(blue dots) denote average positions of CB6 atoms. Since for low eigenvectors axle global movements are not present CB6 rotations are shown by angles with black lines and CB6 expanding/shrinking are shown by dotted circles.	40
3.18	Eigenvector trajectory of CB6 rings of restrained neut state. Colored from starting time frame positions(red dots) to final time frame positions(blue dots) denote average positions of CB6 atoms.	41
3.19	Eigenvector trajectory of CB6 rings of restrained neut state simulated at 350K. Colored from starting time frame positions(red dots) to final time frame positions(blue dots) denote average positions of CB6 atoms.	41
3.20	2 \times 2 polyrotaxane on water surface at 300K.(NVT)	43
3.21	2 \times 2 polyrotaxane in water at 300K.(NPT)	44

3.22	Side view - final simulation time frame PN structure. Transparent vdW models are water(red) and chloroform(blue). The counter ions are added via water substitution and as expected are mainly close to the interface.	45
3.23	Polyrotaxane network in water, chloroform interface.(NPT) Semi-isotropic pressure coupling is used with given pressure matrix equalities. The initial conformation(left) and final conformation(right)	46
3.24	Polyrotaxane network charge states in water-chloroform interface(NPT). From left to right, double layer positive PN, positive PN, neural PN and CB6 absent PN. d_{neut} is the length of x and y axis in the end of 5ns md simulations.	47
3.25	Final largest void free sphere radii of three PN structures.	48
A.1	High Eigenvectors Projected RMSF - Neut System	51
A.2	High Eigenvectors Projected RMSF - Neut System - 350K Temperature	52
A.3	High Eigenvectors Projected RMSF - posr-1 system - 300K Temperature	52
A.4	Low Eigenvectors Projected RMSF - posr-1 system - 300K Temperature	53

List of Abbreviations

MD	Molecular Dynamics
MM	Molecular Mechanics
PDF	Probability Density Function
MIM	Mechanically Interlocked Molecule
pH	potential of Hydrogen
CB6	Cucurbit-6-uril
NVT	Canonical Ensemble
NPT	Isothermal-Isobaric Ensemble
QM	Quantum Mechanics
DFT	Density Functional Theory
LJ	Lennard Jones
PME	Particle Mesh Ewald
FFT	Fast Fourier Transform
SASA	Solvent Accesible Surface Area
RoG	Radius of Gyration
NMR	Nuclear Magnetic Resonance
UV	Ultra Violet
PR	Poly Rotaxane
PN	Poly Rotaxane Network

Chapter 1

Introduction

Understanding the structural properties of organic molecules and molecular systems is and have always been a relevant research area based on their applications in medical fields [1]. There has been a plethora of attempts on utilizing the emergent properties of these multimolecular systems. A subset of these systems that can exhibit unusual degrees of freedom are named Mechanically Interlocked Molecular Architectures [2]. As the name suggests, these types of structures consist of two or more interlocked and not covalently bonded molecules. The topological properties of these molecules allow them to form a structure that is analogous to keys in a keychain, thus to separate them, the keychain must be broken. In this context, the term mechanical bond arises to address the bond between these interlocked non-covalently bonded molecules. Unlike chemical bonds, mechanical bonds allow the molecules to settle in drastically different equilibrium conformations, resulting in tunable but robust architectures that are fairly reminiscent of the idea of molecular machines[3]. There are several examples to these architectures including catenanes, molecular knots, molecular Borromean rings, cyclotides and the one that this thesis is interested in, Rotaxanes[4, 5, 6].

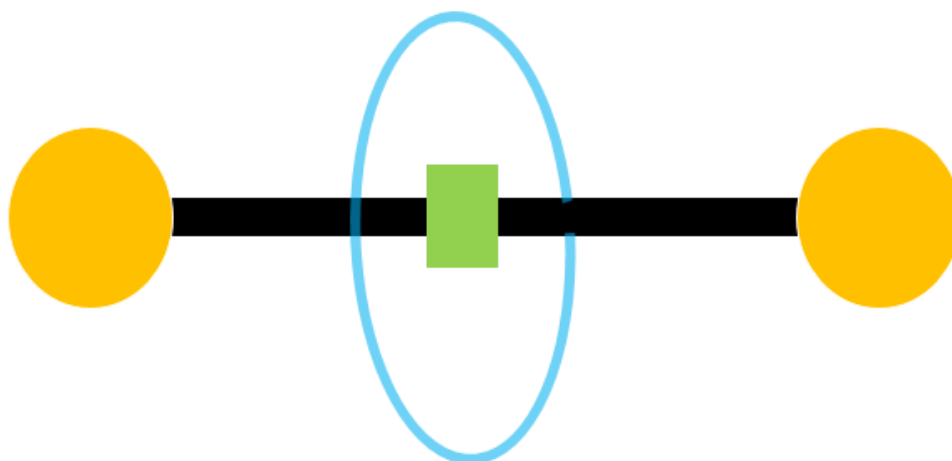


FIGURE 1.1: The basic shape of simplest [2]rotaxane with decoupling preventing groups orange. Green rectangle shows the stable site for the macrocycle.

Rotaxanes are a subclass of MIMs that consist of an axle and a rota(wheel). The most basic rotaxane shape consists of a rod-like axle and a ring torus shaped wheel that is threaded on the axle. The wheel part is not covalently bonded to the axle part and is free to move along the axis if there exists some kind of a driving force[7]. This driving force can range from photon excitation to intensive stirring of the solution containing the rotaxane structures[8]. In the last decade, possible candidates for these driving forces are heavily investigated[9, 10]. One driving force to control Rotaxanes that has a fairly straightforward utilization is valence electron alteration of the system, generally the axle part, via adjusting the pH degree of molecule's environment, namely the solvent[11]. Such stimuli-responsive properties of Rotaxanes has led to novel application such as cell wall destroying kill switches, thin films with data storage capabilities, or ultra stable dyes [12, 13, 14]. While the [2]Rotaxane structure can respond to acid or base addition with rotary and linear motion, due to its rod like shape, the overall behavior is generally limited only to shuttling. To increase the complexity it is possible to synthesize [n]Rotaxane structures where $n > 2$, which has more axles to interact with each other. In literature there are several examples of switchable rotaxanes as it is a rather straightforward way of researching molecular machines[15, 16].

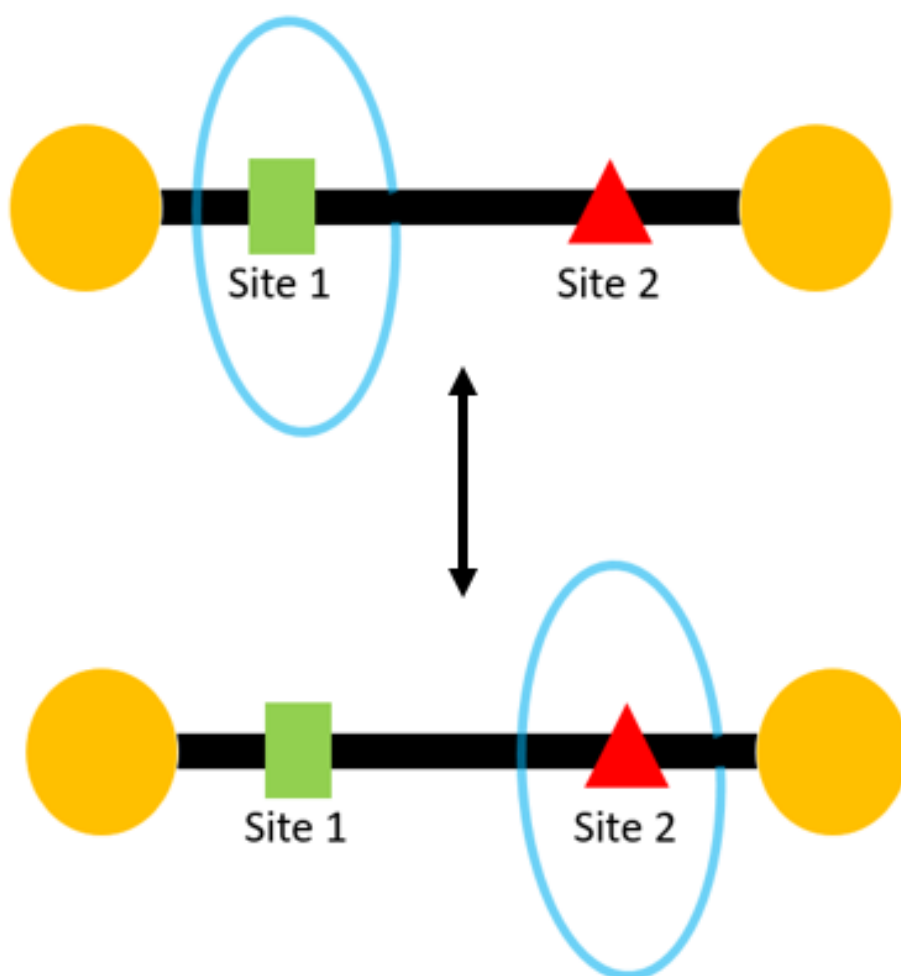


FIGURE 1.2: The basic shape of simplest [2]rotaxane with decoupling preventing groups orange and two stable sites for macrocycle (green, red). A driving force is necessary to move the macrocycle blue, between Site 1 and Site 2

1.0.1 Complex Rotaxanes

Here we simulate and analyze a higher order Rotaxane molecule that can both be synthesized and exhibit useful physicochemical properties. [5]Rotaxane is a tetraphenyl porphyrin core equipped with 4 cucurbit[6]uril (CB6) rings. Cucurbiturils are macrocycles that exhibit different behavior depending on the number of their glycol units denoted by n and can commonly be 5,6,7,8. Among them CB6 shows the ability to catalyze 1,3-dipolar cycloaddition to substituted alkyne and azide substrates by forming 1,4-disubstituted triazoles, which is fundamental to the synthesis of [5]Rotaxane molecule [11,

17]. The axle part, tetraphenyl porphyrin is selected due to their photosensitizer applications. In this thesis, we investigate the pH dependent shuttling behavior of 5-Rotaxane and its network derivative poly-rotaxane molecule via Newtonian Deterministic Molecular Dynamics Simulations.

This rotaxane derivative is chosen because it was shown that, Poryphrin core of [5]Rotaxane attached with ionic groups has cytotoxic behaviour due to generation of reactive oxygen species [18]. It was also demonstrated in recent experiments that CB6 rings of [5]rotaxane can create a screening effect between the medium and triazole groups of porphyrin effectively altering overall macrostructure's toxicity properties [12]. Since main governing interactions between CB6 rings and the poryphrin is mechanic as defined before (i.e., van der Waals and coulomb), it can be hypothesized that CB6 rings undergo a charge-state driven shuttling motion along axes parts. If this hypothesis holds true this dynamic response of CB6 rings if utilized well creates a highly controllable molecular architecture. Notably, introduction of light to the porphyrin complexes is reported to transfer charges along the structure, so our investigation while not concerned with photonic stimuli still can provide some insight on light based activation of rotaxanes.[19].

The experimental data regarding the shuttling motion of this CB6 equipped rotaxane is generally obtained through NMR and UV-Vis spectroscopy with incorporation of an appropriate chromophore [11]. Thus, atomic resolution examination of these charge dependent structural shifts, which can, in this case, be achieved by molecular simulations, can provide further insight on the current applications and further lead to advancements.

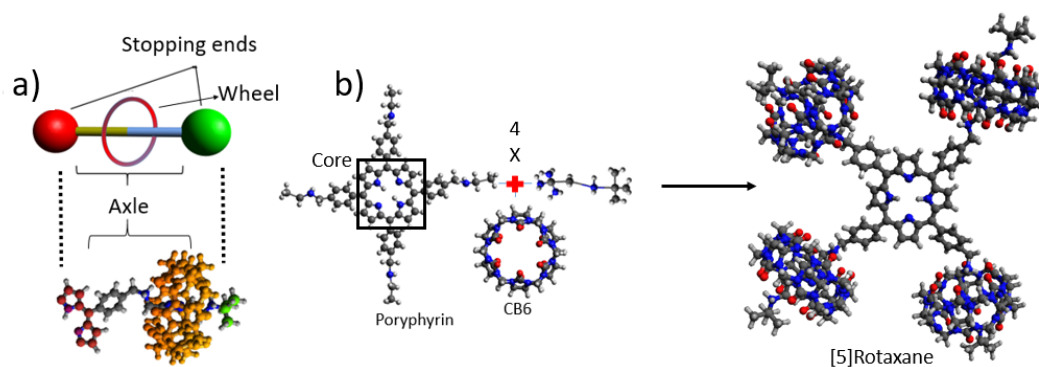


FIGURE 1.3: The mechanically interlocked parts of [5]Rotaxane color coded(a), the components of [5]Rotaxane synthesis(b)

As a continuation, [5]rotaxane structures are demonstrated to show self-assembly properties. It was shown that poly-rotaxane is composed of four [5]rotaxane molecules bonded from end to end and can lead a self-standing thin films [14]. These structures form only in the presence of CB6 rings, and film formation was not observed without rings or with CB7 or CB8. This suggests that CB6 rings somewhat help the molecular arrangement of poly-rotaxanes and enhance covalent bonding between poyphyrin molecules [20]. After investigating the properties of [5]Rotaxane, obtaining the aforementioned poly-rotaxane structure is rather trivial, thus network structure analysis is also done in this thesis. While the network of [5]Rotaxane has different composition, it still maintains light based cytotoxic behavior[20]

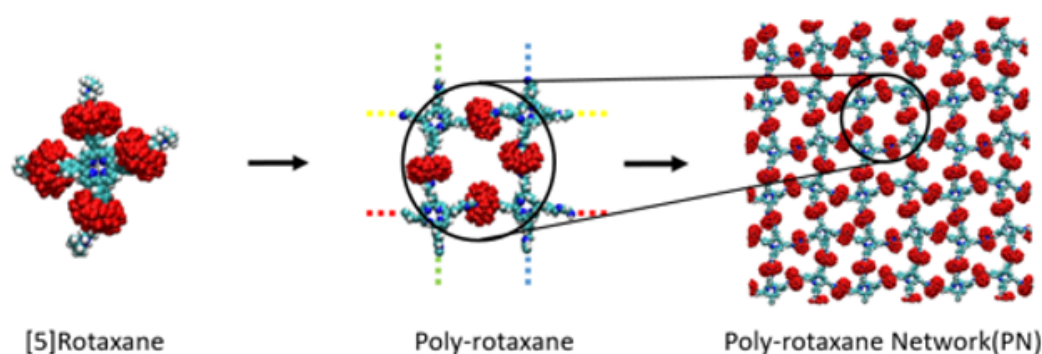


FIGURE 1.4: Supramolecular structures obtained from [5]Rotaxane with periodic boundary bonds. Atoms shown as sphere.

In chapter 2, we lay the basic theoretical and computational foundation of Newtonian dynamics of many body systems. Definition of the key concepts, such as ensembles, scaling micro to macro and the pressure and temperature coupling theory used are discussed. We also explain the computation part by defining the algorithms used with their time complexity, steps of preparing the system and utilization of theoretical statements. The validity of these simulation algorithms on predicting the real life behavior of [5]Rotaxane molecule is discussed in depth here. We continue with describing the framework of atomic interactions namely the MD forcefield. Then in the end we give a brief explanation of all the analysis tools that are used to extract information from our simulations.

Then in chapter 3, we present our plethora of molecular simulations that are of [5]Rotaxane in the solvent of water, concerning the possible charge states

of the [5]Rotaxane and its possible network derivative. Macrostate evolution versus time and resulting conformations at the end of the simulations are examined one by one. Then we utilize the predefined analysis metrics and methods such as the solvent accessible surface area probing and radius of gyration measurements to analyze these conformations and we come to conclusions regarding the physicochemical behavior of [5]Rotaxane and Poly-Rotaxane molecules. Regarding [5]Rotaxane we show that while trademark phenomena of CB6 shuttling is present, it is not symmetric as more than pH stimuli is required to restore the molecule back to its initial state and the supramolecular structure is also altered significantly between charge states. Utilizing these defined metrics, we characterize the interactions between molecular parts and rates of dynamical behavior, such as shuttling, of different protonation states of same molecule. We discuss the findings in correspondence with the experimental data that is in the literature and show that our simulation results agree with experiments.

Finally in chapter 4, we summarize and conclude by assessing the key mechanisms and further research paths. Some derivations and possibly inconsequential data is given in Appendix A.

Chapter 2

Basic Concepts

2.1 Theory

2.1.1 Classical Systems

Theoretical physics of the present day provides a large variety of formulations in the means of representing the physical world. In the scope of non quantum Molecular Dynamics, we draw on the formulations that are discrete, non-relativistic and classical. Using this theory, the equations describing the motion of N particles in a Cartesian reference frame are given by Sir Isaac Newton as:

$$\dot{p}_i = F_i(i = 1, 2 \dots N) \quad (2.1)$$

where \dot{p}_i is the time derivative of momentum of i^{th} object and F_i is the force acting on i^{th} object. Solving only this equations, we can model a system of N non-interacting particles and their dynamical behavior. For a single particle, the frog leap algorithm of calculating the particle trajectory with velocities is given by Verlet as[21]:

$$v(t + \frac{\Delta t}{2}) = v(t - \frac{\Delta t}{2}) + \frac{\Delta t}{m} F(t) \quad (2.2)$$

$$r(t + \Delta t) = r(t) + \Delta t v(t + \frac{\Delta t}{2}) \quad (2.3)$$

where r is the position of the particle and v is the velocity of the particle at a given time. The $\frac{\Delta t}{2}$ term is the reason behind the name of the algorithms because at each iteration r and v are leaping back to back like frogs. The velocity at each time step is obtained as an average quantity, thus the kinetic

energy E_{kin} can also be evaluated at the same instance with:

$$E_{kin} = \frac{1}{2} \sum_i m_i v_i^2 \quad (2.4)$$

In order to mimic the real life systems, in addition to the forces acting on the system, characterization of the constraints are also necessary[22]. For a macro system of balls in a box, constraints to apply can be thought as spring, hinges between balls and physical interactions between balls which restrict the degrees of freedom. In our case, the springs and hinges correspond to atomic bond and angle constraints which are calculated as such and the interaction between balls correspond to non-bonded interactions such as Lennard-Jones potential[23, 24]. The timescale of our simulations, namely Δt , must be at least one order smaller than the magnitude of the vibrational frequencies of the bonds, thus the the time steps are chosen in the scale of femtoseconds to model atoms. The interaction potentials that are used in this work are given as:

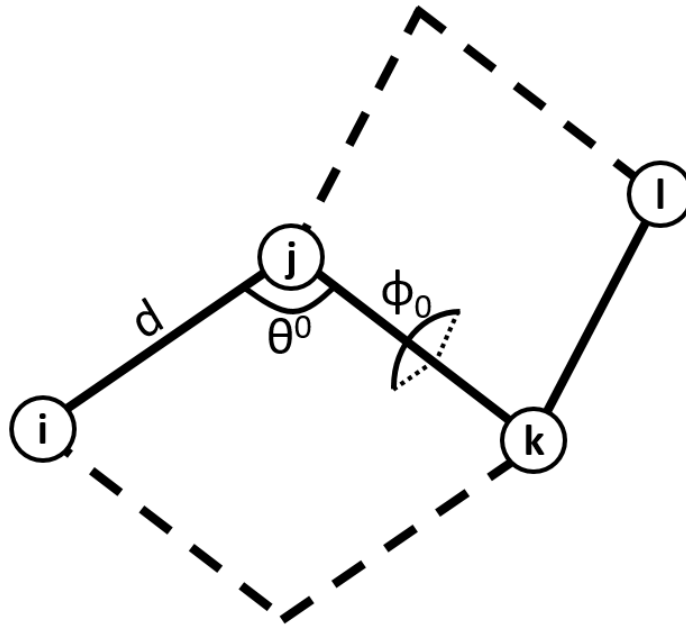


FIGURE 2.1: Spheres are representing atoms, d , Θ^0 and ϕ_0 are equilibrium parameters of the bonded system and any deviation from them creates a force.

$$\text{Bond : } V_i(r_{ij}) = \frac{1}{4}k_{ij}^d(r_{ij}^2 - d_{ij}^2)^2 \quad (2.5)$$

$$\text{Angle : } V_{ijk} = k_{ijk}^\theta (\cos \theta_{ijk} - \cos \theta_{ijk}^0)^2 \quad (2.6)$$

$$\text{Dihedral : } V(\phi_{ijkl}) = k_\phi (1 + \cos(n\phi - \phi_0)) \quad (2.7)$$

with i, j, k, l being the atom indices, V term is the potential, k values are force constants for corresponding equations. Dihedral interactions that only occur in atomic systems where four atoms are bonded together depend on the angle between (i, j, k) and (j, k, l) points' planes are used to model concepts such as torsion. The non bonded interactions that are much weaker and only between two atoms i, j are given as:

$$\text{LennardJones : } V_{LJ} = \frac{C_{i,j}^{12}}{r_{i,j}^6} - \frac{C_{i,j}^6}{r_{i,j}^6} \quad (2.8)$$

$$\text{Coulomb : } V_C = \frac{1}{4\pi\epsilon_0} \frac{q_i q_j}{\epsilon_r r_{ij}} \quad (2.9)$$

where r is the distance between atoms, C is a constant depending on atom type, ϵ_0 is the permittivity of vacuum, ϵ_r is the reaction field parameter dielectric constant and q is the charge of the particle.

In order to obtain the macro state properties of the system such as temperature and pressure, one must bridge the gap between individual atoms moving in a box and some water in a container. This bridge is constructed by Ludwig Boltzmann and J. Willard Gibbs as an equation that relates a macro state with corresponding micro states[25].

$$S = -k_b \sum_i p_i \ln p_i \quad (2.10)$$

Entropy named by S or H in the case of information theory is a measurable property that is associated with a state of randomness or disorder. The equation 2.10 in the absence of the Boltzmann constant k_b , defaults to Shannon Entropy that gives the average level of information of random variable's possible outcomes[26]. It is possible to obtain the right side of the equation only by using our micro definitions. Once we have obtained the micro definition of the system, Maxwell relations coupled with thermodynamic potentials, a set of thermodynamics equations allows us to calculate the aforementioned macroscopic properties[27].

$$\mu_{tot} = \sum_i \mu_i N_i \quad (2.11)$$

$$dU = TdS - PdV + \mu_{tot} \quad (2.12)$$

$$dF = -SdT - pdV + \mu_{tot} \quad (2.13)$$

$$dG = -SdT + Vdp + \mu_{tot} \quad (2.14)$$

$$dH = TdS + Vdp + \mu_{tot} \quad (2.15)$$

where μ is the chemical potential, U is the internal energy, F is the Helmholtz energy, G is the Gibbs Energy, H is the enthalpy, V is the volume, P is the pressure, S is the entropy and finally N is the particle number[28, 29]. One can traverse through equations 2.12 to 2.15 with repeated Legendre Transformations[30].

There are certain strong assumptions to make in order to describe a physical system in the language of statistical mechanics such as the system having large number of particles[31]. A major assumption is: For systems that are isolated, at a certain energy and composition, equal a priori probability postulate states that the system can be found with equal probability in any

microstate satisfying that knowledge. This thought leads to the formulation of statistical ensembles.

2.1.2 Micro to Macro

An important building block in this theory that has strong connections with postulate of a priori equal probabilities is the microcanonical ensemble[32]. The microcanonical ensemble is one of the statistical ensembles where each possible state of the system has a definite and exact total energy. The primary macroscopic variables of this system, N (number of particles), E (total energy), V (volume) are assumed to be constant, so this ensemble is sometimes called NVE ensemble. Maximizing the gibbs entropy for discrete systems where sum is over all microstates Ω with energy constraint using Lagrange multiplier method, we get:

$$L = -k_b \sum_i p_i \ln p_i - \lambda \sum_i p_i \quad (2.16)$$

solving $\frac{\partial L}{\partial p_i} = 0$ for p_i gives:

$$p_i = \frac{1}{\Omega} \quad (2.17)$$

finally plugging this probability back into the Gibbs Entropy formula:

$$S = -k_b \sum_i \frac{1}{\Omega} \ln \frac{1}{\Omega} \quad (2.18)$$

gives the rather familiar expression of Boltzmann entropy:

$$S = k_b \ln \Omega \quad (2.19)$$

While NVE ensemble is useful for describing simple systems, it is not preferred for describing non trivial real life systems because of not allowing energy fluctuations resulting in every microstate having the same probability $\frac{1}{\Omega}$. If we remove the constraint of defining an exact total energy for the states of the system by adding another term to the Lagrange multiplier equation, a more preferable ensemble for modeling real life systems is obtained[33]. We can derive canonical ensemble by adding the term:

$$\bar{E} = \sum_i E_i p_i \quad (2.20)$$

and again solving for $\frac{\partial L}{\partial p_i} = 0$ for p_i gives way to a probability that depends on the energy of the state:

$$p_i = \frac{\exp \frac{-\beta E_i}{k_b}}{\sum_i \exp \frac{-\beta E_i}{k_b}} \quad (2.21)$$

where β is the reciprocal of the temperature T . After defining microscopic definition of our system with the theory of canonical ensemble, the denominator of the equation 2.21 partition function Z allows us to extract the macrostate information via:

$$U = -\frac{\partial \ln Z}{\partial \beta} \quad (2.22)$$

While we have defined this partition function for a discrete system, the continuous classical system counterpart follows a similar logic of summing the Boltzmann factors $\exp \left(-\frac{\beta E_i}{k_b} \right)$ continuously over all microstates, namely the phase space, given as:

$$Z = \frac{1}{h^{3N} N!} \int \exp \left(\frac{-\beta E(x, p)}{k_b} \right) dp dx \quad (2.23)$$

where x and p are position and momentum respectively and h is the planck constant there to simply make the partition function Z unitless.

With this theory, we can fully simulate systems that has constant volume, temperature and particle number, namely NVT ensemble systems. While there are many isochoric systems, our concern in vivo systems and systems that are in contact with the atmosphere are all isobaric. So as a final modification to the canonical ensemble, we must keep the pressure constant instead of the volume[34]. We plug in the ensemble parameters P and V to the generalized Boltzmann distribution, which holds for canonical, grand canonical and isothermal-isobaric ensembles, to obtain the NPT ensemble partition function as[35]:

$$Z_{npt} = \int Z(NVT) \exp(-\beta PV) \beta P dV \quad (2.24)$$

Summing up, we now can calculate macrostate variables of systems that are in thermal equilibrium that have constant particle number and either constant pressure or volume. Conversely, initialization of a system with desired temperature and pressure can be achieved with random sampling of particle kinetic energies from the obtained maximum entropy probability distribution that is obtained by solving the canonical partition function for ideal gases. In our case of constant temperature simulations, the initial velocities are generated from:

$$p(v_i) = \sqrt{\frac{m_i}{2\pi k_b T}} \exp\left(-\frac{m_i v_i^2}{2k_b T}\right) \quad (2.25)$$

Since the resulting total kinetic will not fully correspond to the required temperature T due to the center of mass motion, a correction of removing the center of mass motion of the system is made, then all velocities are scaled to make the correspondence exact.

2.2 Molecular Dynamics

2.2.1 Methodology

In classical molecular dynamics simulations, the particles are thought as infinitesimal point objects that interact with each other. There are several approaches depending on the sizes of systems that are being investigated. For large systems such as cell walls and peptides, coarse grain models are preferred, since it is not possible to model and simulate large systems in every individual atom basis[36]. On the other hand for smaller systems of molecules such as [5]Rotaxane in water, atomistic resolution simulations are useful[37]. The theoretical definition and of our systems that are given in the previous section can now be utilized with to create a computational method to simulate the movement of atoms while keeping macrostate variables such as temperature and pressure, accurate. One vital benefit of simulating the "movement" over other modeling methods is that the dependence of the atoms spatial behavior on the initial configuration is low, since with coupling kinetic energy the system can overcome potential barriers, resulting in the same converged final configuration regardless of the initial structure. There are several algorithms in play in order to both make the simulations feasible and realistic.

Firstly, temperature and in the case of NPT, pressure couplings of the system are quite vital. There are several P and T coupling algorithms with different benefits, a relatively straightforward approach of constant T and P simulations is formulated as Berendsen T and P coupling[38].

$$\frac{dT}{dt} = \frac{T_0 - T}{\tau} \quad (2.26)$$

$$\frac{dP}{dt} = \frac{P_0 - P}{\tau_p} \quad (2.27)$$

where τ, τ_p is the time constant of coupling and is used to modulate how fast the system T or P deviation decay from bath T_0 or P_0 values. The idea using these coupling algorithms is to correct the fluctuations of kinetic energy, effectively simulating a system that is in contact with a heat bath and/or a piston for NPT ensemble. For Berendsen T coupling algorithm the kinetic energy fluctuations are suppressed and the deviation of system temperature from previously defined T_0 is slowly corrected according to the given equations. This fluctuation disallowance prevents the system from reaching true canonical ensemble, which in turn affects fluctuation properties such as heat capacity, especially in smaller systems like our [5]Rotaxane since the error scales with $\frac{1}{N}$. In order to address this, in our MD simulations we utilize a modified Berendsen Thermostat(Velocity Rescaling) for T modulation given by:

$$dE_{kin} = (E_0 - E_{kin})\frac{dt}{\tau_T} + 2\sqrt{\frac{E_{kin}E_0}{N_f}}\frac{dW}{\sqrt{\tau_T}} \quad (2.28)$$

Here we modulate the kinetic energy by essentially adding a Wiener process scaling W with the number of degrees of freedom N_f term to obtain the correct canonical ensemble with fluctuations while keeping the decay of temperature deviations[39]. A likewise argument could be made for Berendsen P coupling algorithm on not generating an exact NPT ensemble, thus causing errors on small systems. The mechanism behind pressure modulation is altering the box dimensions while obeying matrix equations of motion. In this instance we use an algorithm called Parrinello-Rahman pressure coupling[40]. The equation that box vectors b must satisfy reads:

$$\frac{db^2}{dt^2} = VS^{-1}b'^{-1}(P - P_0) \quad (2.29)$$

where V is the box volume and S is the matrix parameter of strength of coupling. Unlike the previous P coupling algorithm, Parinello-Rahman is more

accurate in small systems. Our systems are constant pressure since the molecular structures are synthesized in beakers that are open to air, thus we mainly use constant pressure coupling while constant volume method is used for equilibration purposes. In order to calculate the pressure of each direction we utilize the virial tensor of our system:

$$\Xi = -\frac{1}{2} \sum_{i < j} r_{i,j} \otimes F_{i,j} \quad (2.30)$$

summed over tensor product of position of and force acting on particle pairs i, j used to calculate the pressure tensor as:

$$P = \frac{2}{V} (E_{kin} - \Xi) \quad (2.31)$$

In isotropic systems we can calculate the scalar pressure for total of 3 axes with $tr(P)$ since axes are coupled. For temperature and pressure values, we chose a standard 300K and 1 atm to simulate systems that are examined for steady state properties. For kinetical property simulations, we vary the temperature up to 350K to force molecular movement and semi-isotropic pressure coupling is utilized for Polyrotaxane network simulations.

2.2.2 Forcefield

The constant parameters of atom-atom interactions (eqn. 2.5) are taken from parameter sets called forcefields. The parameters in the forcefield for a chosen energy equation may be derived from experiments, calculations in quantum mechanics such as DFT or both. In the computation step there are some considerations for feasibility, namely to reduce the cost of computation, mainly for long range interactions. Since both Coulomb and LJ forces can be calculated regardless of the distance, we must introduce a cutoff range or use generalizations to skip computing every pair of interactions[41]. A well known and utilized method to resolve Coulomb calculations in periodic systems is Ewald sum electrostatics[42]. The total electrostatic energy of all the particles and their periodic images in the N particle periodic system is given by:

$$V = \frac{1}{4\pi\epsilon_0} \sum_{n_x} \sum_{n_y} \sum_{n_z} \sum_i^N \sum_j^N \frac{q_i q_j}{r_{ij,n}} \quad (2.32)$$

with $n = (n_x, n_y, n_z)$ box index vector. While this sum is conditionally convergent, it does very slowly, thus we instead divide the energy term for

short and long range interactions. Exploiting the periodicity property of long range interactions and assuming neutral system with each point charge is screened by a diffuse cloud of opposite charge, we can convert the long range part of sum to the reciprocal space via Fourier transformation[43].

$$V_{long} = \frac{1}{4\pi\epsilon_0} \frac{1}{2\pi V} q_i q_j \sum_{m_x} \sum_{m_y} \sum_{m_z} \frac{\exp(-(\pi m / \beta)^2 + 2\pi i m \cdot (r_i - r_j))}{m^2} \quad (2.33)$$

where $m = (m_x, m_y, m_z)$ and β is the relative weight of long range sum. Even this model has a time complexity of $O(N^2)$ thus not very applicable for large systems. One final modification to the reciprocal term is using the Particle Mesh Ewald(PME) algorithm proposed by Tom Darden[44]. PME algorithm assigns charges to a grid using interpolation instead of summing wave vectors of reciprocal part directly. The converted grid sum is much faster to compute via 3D Fast Fourier Transform(FFT) algorithm, resulting in a time complexity of $O(N \log(N))$.

Depending on the details of the simulation and the system that is being analyzed, all these aforementioned interactions defined in this force field section can be modified to address the requirements of your model and holonomic constraints can be added to prevent unwanted behavior or save computation cost. A small atomistic system would require much higher precision(lower error) for short range and long range interactions(i.e. shift functions) in terms of calculation algorithms, which in turn increases the computational cost, while for coarse grained models, such precision is both unnecessary and infeasible. Thus in this section we were only concerned with the main picture and methods that are used in our simulations.

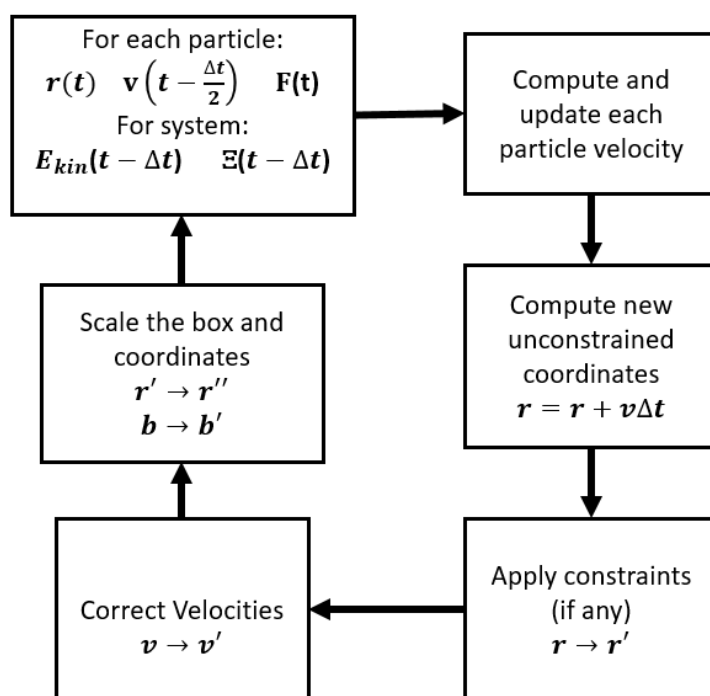


FIGURE 2.2: Given particle positions r , velocities v and force acting on each particle F , the algorithm of updating the system through time trajectory.

2.2.3 Analysis

Now that we have a full description of our system in terms of all the macro and micro considerations, we define the analysis tools/approaches that are used to extract information from both the simulation time trajectory and final obtained conformation. Starting with the most essential visual inspection methods, we define the metrics utilized in this work with reaction coordinate dependency, namely solvent accessible surface area, radius of gyration, interaction energy, hydrogen bonding, average distance analysis, essential dynamics analysis[45, 46, 47, 48].

Solvent accessible surface area(SASA) measurement is a useful tool to inspect the properties of solvent molecule interactions. In our case of [5]Rotaxane, the collapsible nature of the molecule creates distinct phases that can be differentiated by measuring their relative. Also as the phase transition occurs, as we will see in chapter 3, the SASA change is directly analogous to the rate of phase transition. To compute SASA, we probe the van der Waals surface of

our molecule with a sphere of a given radius. As we are interested in water-molecule interaction properties, we use 0.14nm radius sphere, approximately the radius of a water molecule[49].

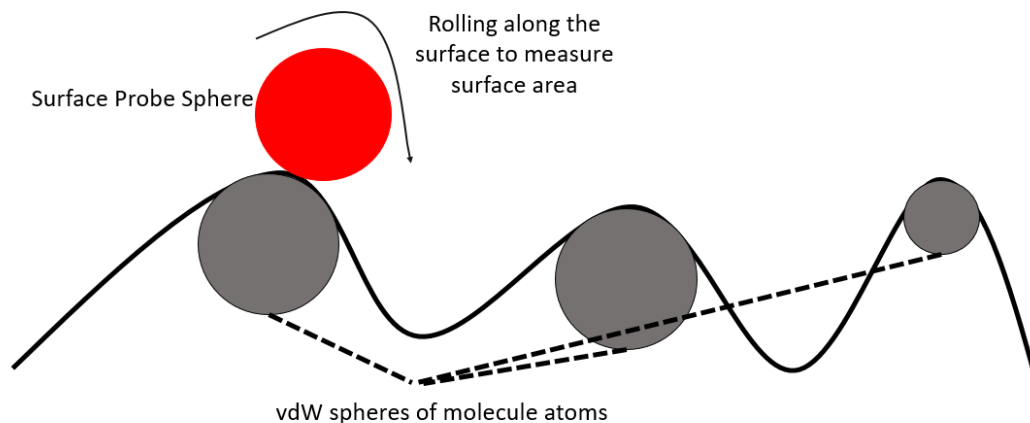


FIGURE 2.3: 2D representation of surface probing to calculate solvent accessible surface area. The radius of the probing sphere effect the final SASA result.

Here, as with many analysis calculations in MD, we are more interested in the change in SASA compared to the steady state values. For a "foldable" molecule such as [5]Rotaxane, a sharp drop in SASA would correspond to the change of molecule into a ball like shape with closely interacting sites, preventing the probing sphere from touching the central parts of the collapsed structure.

Another measure that is closely related to the molecular size and shape is radius of gyration(RoG) much simpler to calculate than SASA, given by:

$$R_g^2 = \frac{\sum_i |r_i^2| m_i}{\sum_i m_i} \quad (2.34)$$

where R_g is the radius of gyration, m_i is the mass of atom i and r_i is the position of atom i with respect to the center of the mass of the molecule. RoG is the root mean square distance of the molecule's atoms from its center of mass, thus a higher RoG value indicates a more spread molecule. In this context, RoG is also used as a measure of molecular size, however it does not correlate with SASA fully for mechanically interlocked molecular architectures as the movement of the macrocycle part generally affects one metric more than the other as we will see at the results section.

Hydrogen bonding is an interaction that occurs between a hydrogen that is covalently bonded to a more electronegative atom (e.g. oxygen for water) and another atom with a lone pair of electrons. We quantify the hydrogen bonding between the solvent and molecule by counting the donor-acceptor pair distances and angles that fit the criteria of forming hydrogen bonds. [5]Rotaxane molecule have CB6 ring oxygens, axle nitrogens and central nitrogens as possible hydrogen bond donors. The quantification is done on each timestep of the simulation trajectory.

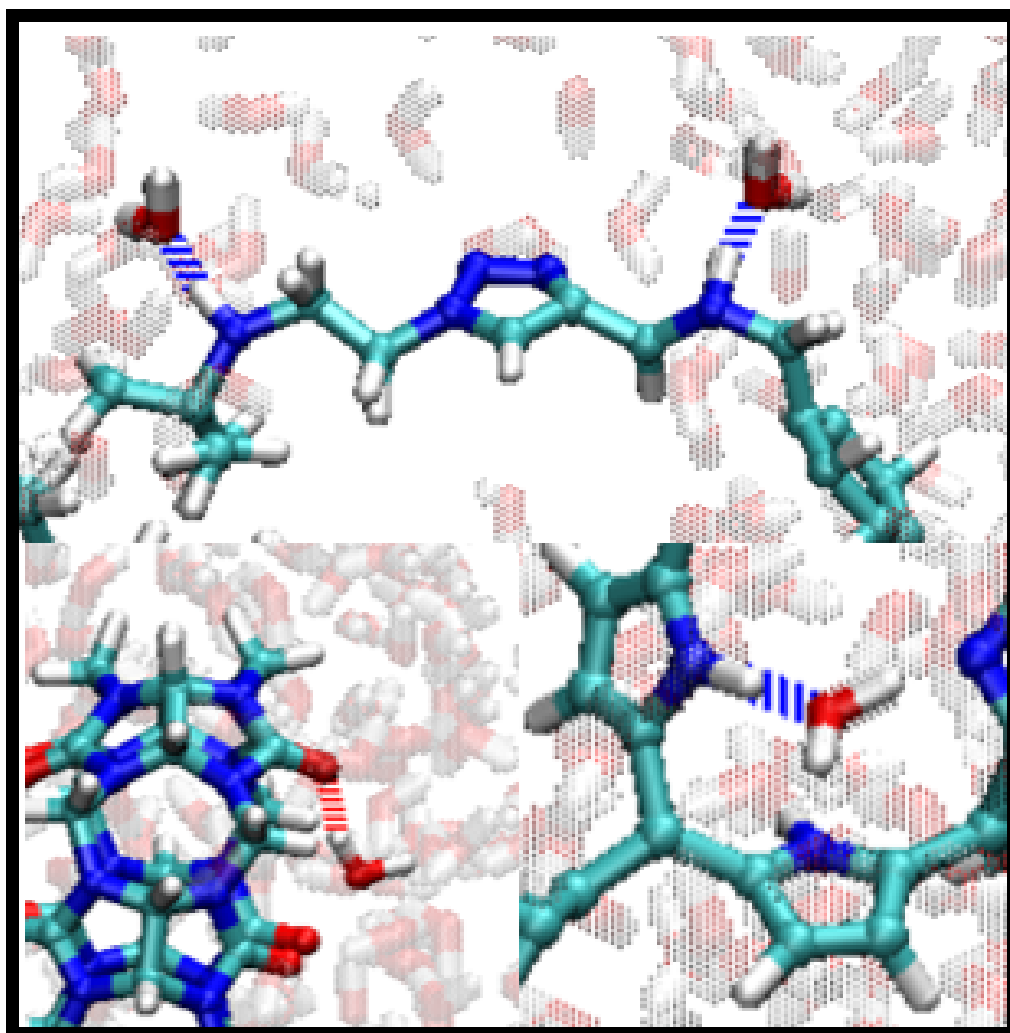


FIGURE 2.4: Electronegative nitrogen groups hydrogen bonding with water atoms are shown as dashed blue lines, oxygen groups are shown as dashed red lines(bottom-left).

Finally another method that we must describe in depth is the covariance analysis of temporal positions of atoms. As the atoms move with a correlated

trajectory correspond to macromolecular movements such as translation and rotation, essential dynamics analysis of the system proves to be useful for the means of isolating local movements such as the so called macrocycle "shuttling". We can write the covariance of positions of the atoms as:

$$C = cov(r)_{i,j} = \langle (r_i - \langle r_i \rangle)(r_j - \langle r_j \rangle) \rangle \quad (2.35)$$

where C is a $3N \times 3N$ matrix that can be diagonalized with transformation matrix T given as:

$$D = T'CT \text{ and } tr(D) = \sum_i \lambda_i \quad (2.36)$$

with λ_i being the i^{th} eigenvalue and T the matrix of eigenvectors. We can project the eigenvectors on to the trajectory with vectorized operations to obtain principle components $p(t)$:

$$p(t) = T'(r(t) - \langle r \rangle) \quad (2.37)$$

and finally we model the i^{th} principle component on the visual trajectory to see the isolated movements. As the first principle modes generally correspond to global motions, we skip them and filter the trajectory along the other principle modes to see non global movements clearly.

Chapter 3

Molecular Dynamics Simulations of [5]Rotaxane

3.1 Simulation Details, Results and Discussion

For the parametrization of [5]Rotaxane, the bonded parameters of CB6 rings are taken from Automated Topology Builder(ATB) Repository and the parameters of porphyrin core are obtained from GROMOS-54A7 element-wise bonded interaction coefficients[50, 51]. After the parametrization, 5 different protonation state structures of [5]Rotaxane is prepared corresponding to 5 different pH values. SPC model water is used as the simulation medium. All simulations are done with identical initial box dimension initialization keeping the box boundary at least 2 nm away from the molecule with periodic boundary conditions. The temperature values are selected as 300K for equilibrium state simulations with 0.1 ps V-rescale coupling time constant and in order to examine the rate and spontaneity of shuttling, temperature coupling to 350K is also used. For [5]Rotaxane molecules, pressure is always kept constant at 1 bar via altering the box dimensions accordingly with 0.2 ps Parinello-Rahman barostat coupling time constant. Only on simulations of non interface surface structures, constant volume conditions NVT are used. All systems are run up to 16 ns with 3 fs step size for equilibrium simulations. The stability of each configuration is questioned by extending each simulation up to a total of 30 ns. For each system of equilibration, 5 replicas are run. For system that are initialized for the purpose of measuring kinetic transition properties, 20 replicas are run. All equilibrium simulations start from different protonation, non collapsed(axles not bent towards center) structures of [5]Rotaxane molecule.

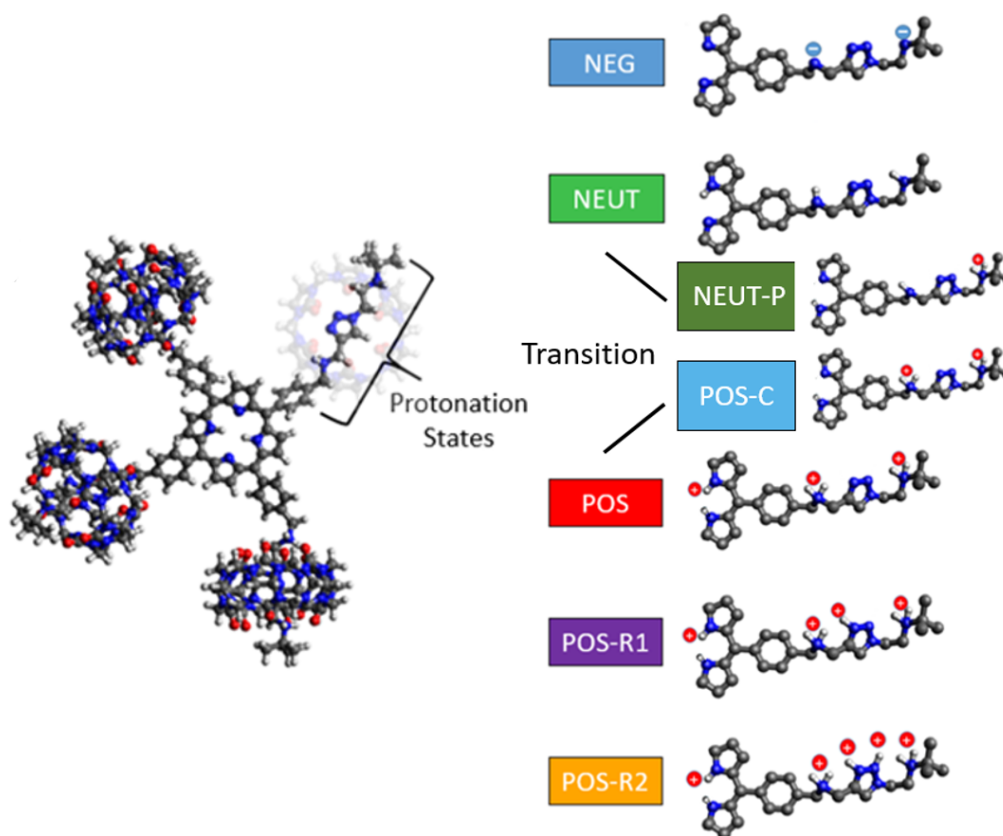


FIGURE 3.1: Five different charge states and two transition states corresponding to different pH values, for the remainder of this section they will be referred as neg(negatively charged), neut(neutral), neut-p(outer protonated axle), pos-c(axle positively charged), pos(axle and core positively charged), pos-r1(axle, core and centermost triazole nitrogen positively charged) and pos-r2(axle, core and triazole positively charged)

Out of these charge states(Fig.3.1) neut, neut-p, pos-c pos are obtainable experimentally, while neg, pos-r1 and pos-r2 states are simulated as exotic conformations that are highly unlikely to be obtained experimentally but could very well be utilized to obtain information on the dynamical properties of CB6 porphyrin interactions.

3.1.1 Charge Assignment

The charge distribution of the base structure (poryphyrin) when equipped with CB6 rings is the determining factor on the final shape of the molecule. As the wildly different possible molecular conformations of complex [5]rotaxane provides significantly different charge distributions (up to 0.1e) on carbon atoms when calculated with geometrical QM methods, nitrogens being the donor atoms on the axle and core part, are selected as the only sites to modify [52, 53, 54]. Nitrogen-hydrogen pairs are assigned a charge that is taken from the similar structures in GROMOS96 54a7 force field, while keeping the whole structure neutral. To further crosscheck the correctness of assigned partial charges, Electronegativity Equalization Method, a fast charge computation comparable to ab initio is used to compute and compare the individual charges of all atoms in the poryphyrin molecule. As the partial charges of individual atoms are highly dependent on the molecular geometry, protonation state and CB6 positions, this simplistic approach is adopted to be able simulate redox reactions. When we traverse above the neut state to create a positively charged molecule, the added hydrogen atom's charge is not distributed along the molecule and always kept at +1 e as the redistribution is also highly dependent on geometry. Throughout each simulation, point charges of each atom does not change, and each charge is neutralized by its solution-phase counter ion, due to the PME algorithm.

	NEG	NEUT	POS	POSR	POSR2
N	-0.9225	-0.31	-0.31	-0.31	-0.31
NL	-0.31	-0.31	-0.31	-0.31	-0.31
NT	0.0	0.0	0.0	0.0	0.0
HN	N/A	0.31	0.31	0.31	0.31
HP	N/A	N/A	1.0	1.0	1.0
HT	N/A	N/A	N/A	1.0	1.0

TABLE 3.1: Charges assigned to individual nitrogen and hydrogen atoms.

N - amine group nitrogens on the axle parts,
 NL - protonated nitrogens on center porphyrin core,
 NT - triazole and non protonated core nitrogens,
 HN - hydrogens of N,
 HP - hydrogens added to N for protonation,
 HT - hydrogens added to triazole NT

3.1.2 Configuration of single [5]Rotaxane

We quantified configurational properties of [5]rotaxane structures by analysing equilibrium structures that we obtain at the end of the simulations using aforementioned techniques (Chapter 2) with at least 10 ns-long simulation times. We considered five charge states of [5]rotaxane as described in Fig.3.1 and refer, for the remainder of this thesis, to these states as follows; negatively charged (neg), neutral (neut), positively charged (pos), a second positively charged but with additional charges on triazole groups (pos-r1) and finally with fully protonated triazole groups(pos-r2). These states are chosen to fully investigate the protonation dependency of final molecular conformation and CB6 positions. The expected behavior here for CB6 rings, as given in the literature, is them residing on less protonated nitrogen terminals, avoiding high protonation sites.

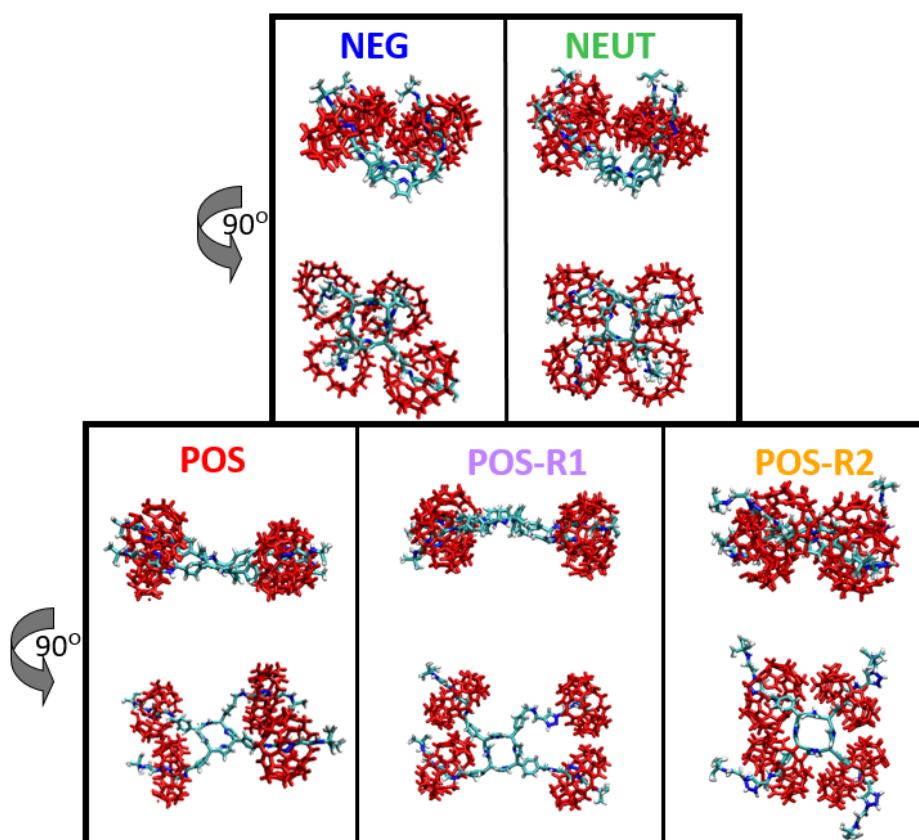


FIGURE 3.2: Final conformations of different Rotaxane charge states. The protonation increases from top to bottom. First and last neg and pos-r2 states are the exotic states that are unlikely to be obtained experimentally.

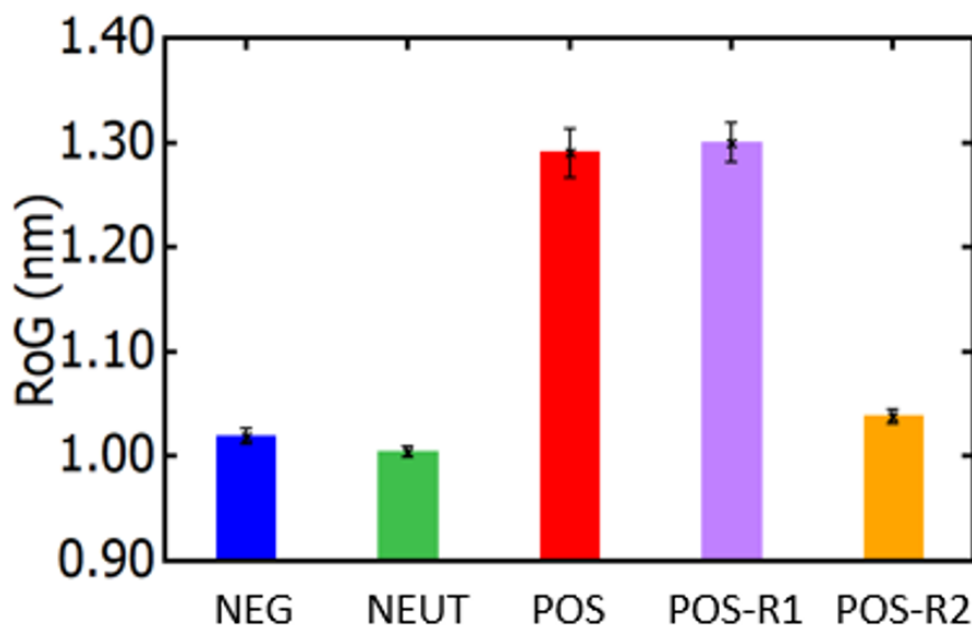


FIGURE 3.3: Radius of gyration of charge states averaged over time and replicas.

At first look, the radii of gyration (RoG) of [5]rotaxane do not exhibit a significant difference with variations in the molecule's charge state except for pos and pos-r1 state: the RoG values lie around $R_g \sim 1$ nm for the neg neut and pos-r2 charge state that we consider here (Fig. 3.3). Notably, the [5]rotaxane pos and pos-r1 state (i.e., pos, pos-r1 case also defined in Fig. 3.2), shows higher RoG values than other cases. Contrarily, the charge state with zero net charge on the axle parts corresponds to the smallest RoG. A visual inspection of our equilibrium-simulation snapshots reveals that molecular configurations are vastly different for each charge state (Fig. 3.2). Notably at pos-r1 state, although CB6 move away from the core, the RoG responds very weakly. This is due to the axle bending of the corresponding shuttled axle towards the core reducing the overall RoG. We observe that the location of CB6 directly affects the axle mobility.

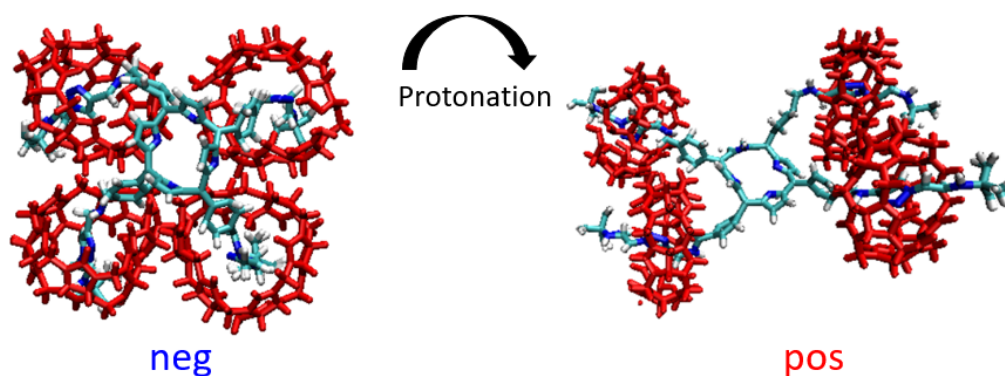


FIGURE 3.4: Drastic conformational change between non charged(neg) and positively charged(pos) states.

Relative orientation of porphyrin arms (porphyrin core + axle parts) are highly-charge dependent; in our neutral (i.e., neut) and negatively charged (i.e., neg) systems, four CB6 rings are positioned in a way that porphyrin core is highly exposed to water molecules but in an asymmetric fashion (Fig. 3.2). This configuration is achieved by bringing CB6 rings closer while keeping their average position near the corresponding triazole group (Fig. 3.2). As interacting CB6 pulls axes towards the center, they also prevent axle positions from fluctuating greatly also indicated by much lower standard errors (Fig. 3.3). Contrarily, for pos and pos-r1 states, CB6 rings interact with each other in the groups of two, resulting in an open [5]rotaxane conformation with a relatively larger R_g value (Fig. 3.3). The most drastic configuration shift occurs in pos-r2 state; in this state, CB6 rings are positioned near the center of the [5]rotaxane, effectively reducing RoG with a distinctly different mechanism than those occurred for the neg and neut states. All states are highly stable when the simulations are extended beyond 10 ns.

In general, pos-r1 and pos-r2 states show CB6 action along the axles, in which for pos-r1 at least two of the four CB6 rings stay on triazole while other two shuttle away from the core and for pos-r2 all four CB6 rings shuttle towards center. We observe this trend in 20 different simulations, each of which was initiated with a different initial velocity distribution realizations (Fig. 3.2). We will discuss the motion of CB6 rings further in the following sections.

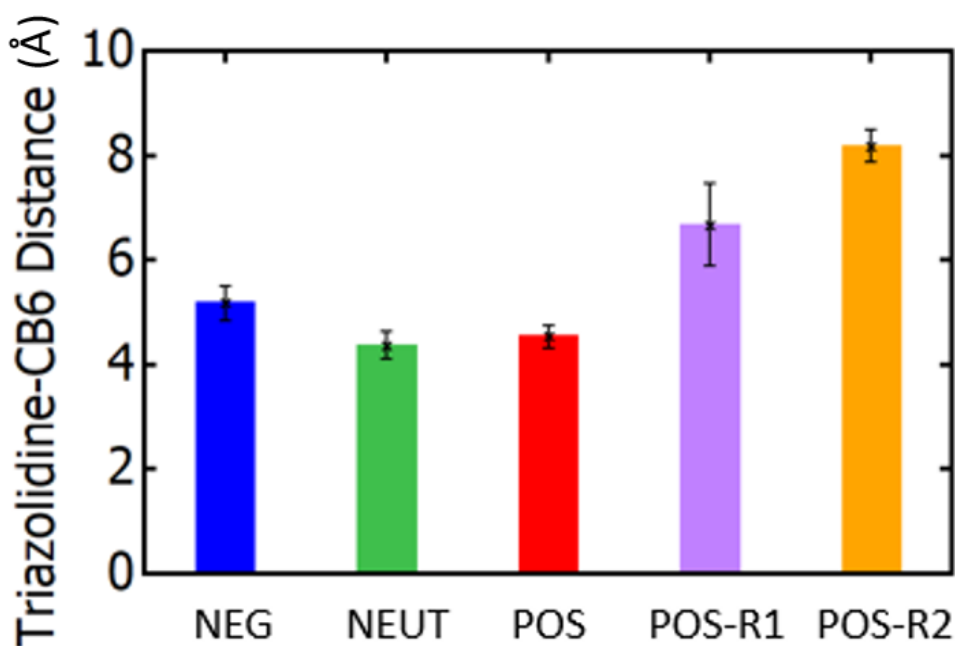


FIGURE 3.5: CB6 and corresponding axle Triazole distances of charge states averaged over time and replicas.

Given that in each charge state, average positions of CB6 rings are major determinant of the overall molecular configuration, we analyzed the average optimum positions of the rings. In simulations, the stable average position for CB6 rings appears to be on 1,2,3-triazole groups since the positive charge except at the state pos-r1 and pos-r2 (Fig. 3.2), following the trend of CB6 not preferring positively charged sites. This can be also seen in Fig. 3.5, in which the average distance between the centers of mass of triazole and CB6 rings for the five charge states is plotted. For all cases except, pos-r1 and pos-r2, the two groups are in close physical proximity, consistent with the equilibrium configurations in Fig. 3.2. Thus, we conclude that charge state do not effect the location of the rings if triazole groups are not protonated. Secondly, the CB6 rings are repelled from both positively or negatively charged terminals, suggesting the role of steric interactions keeping [5]rotaxane molecule intact while allowing a positional flexibility to its rings.

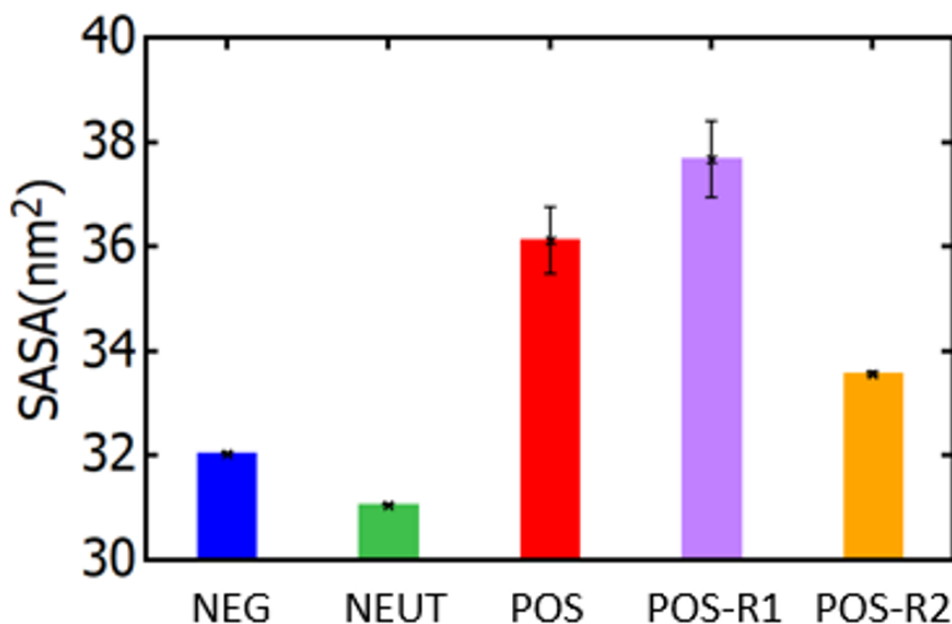


FIGURE 3.6: Solvent accessible surface area of different charge states average over time and replicas.

To gain further insight on the molecular interactions leading to various [5]rotaxane conformations, we quantified the molecular configurations by calculating the solvent accessible surface area (SASA) and hydrogen bonding between solvent and the molecules for each charge state (Fig. 3.7). A higher SASA value is an indication of stronger interactions with solvent molecules [55]. Consistent with the visual analyses, the pos-r1 state protonation of triazole rings greatly increases the SASA by placing the CB6 rings away from the core porphyrin. In our neutral and negatively charged systems, the SASA values are the smallest due to the folding of axle parts and increasing interactions between CB6 rings. For the pos-r2 case, all the CB6 shuttle towards center, effectively reducing both SASA and RoG.

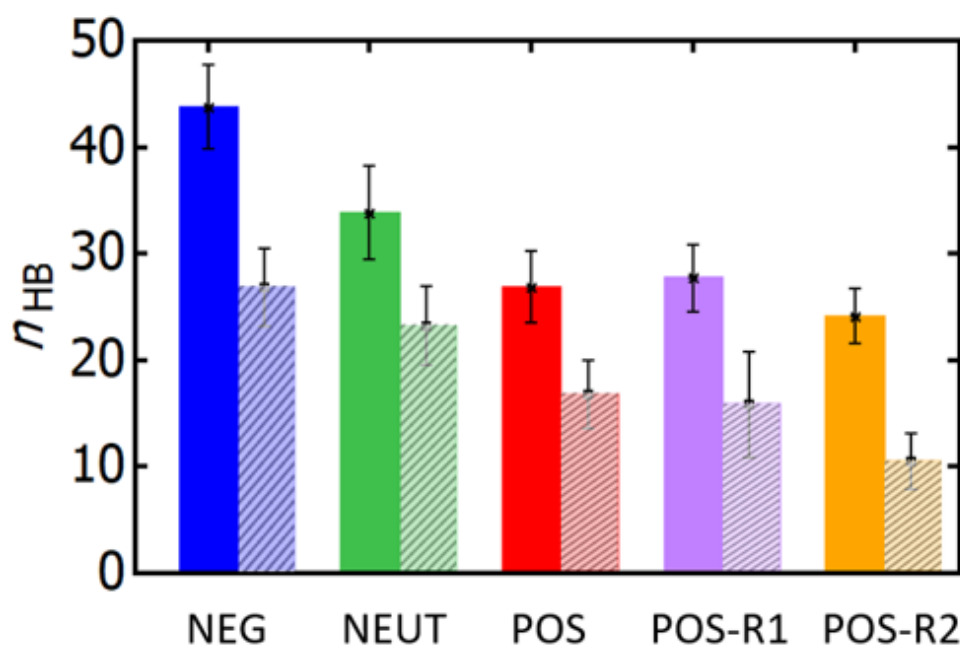


FIGURE 3.7: Hydrogen Bonding of different charge states averaged over time and replicas. The adjacent dashed bars correspond to water - CB6 contribution.

Hydrogen bonding between the solvent and components of [5]rotaxane also exhibit a strong dependence on the charge state of [5]rotaxane. The general trends is that as the protonation of the [5]rotaxane increases, the total number of hydrogen bonding n_{HB} with solvent decreases (Fig.3.7). The maximum number of hydrogen bonding is observed for the neg state with $n_{HB} \approx 44$ while the minimum is $n_{HB} \approx 24$ for the state pos-r2. Interestingly, the contribution of CB6 rings to the total hydrogen bonding decreases as protonation is increased. Porphyrin hydrogen bond contribution mainly comes from axle nitrogens regardless of the state. Relative contributions of porphyrin and CB6 do not change and are about 50% within the error bars. This suggests that the close arrangement of CB6 rings away from the core not only blocks the ability of the porphyrin to establish hydrophilic interactions but also limit the hydrogen bonding capacity of freestanding CB6 groups. This situation is opposite in the negatively charged and neutral [5]rotaxane moieties; despite the close arrangement of CB6, their positioning away from the core on the axle and exposed negative charge of N atoms in the absence of extra hydrogens allow them to form more hydrogen bonds.

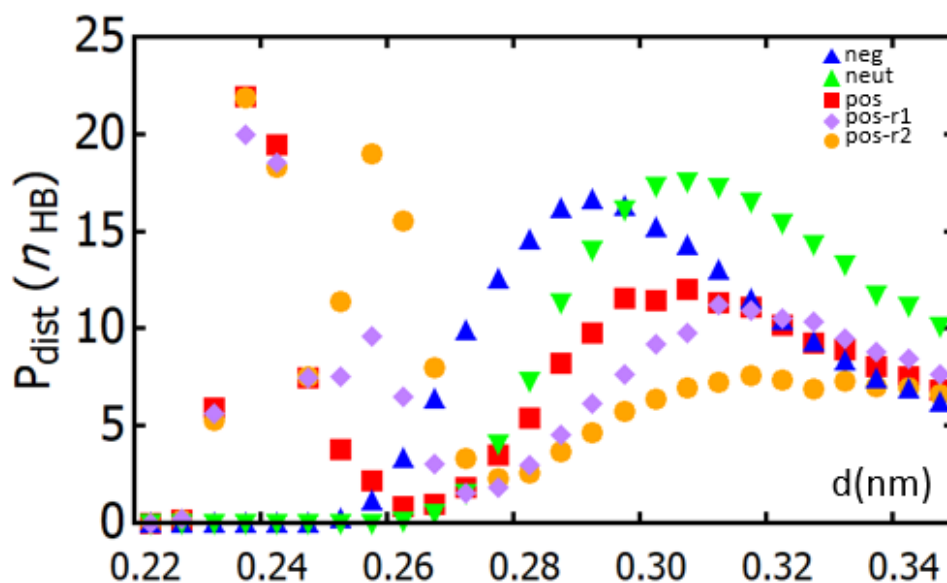


FIGURE 3.8: Hydrogen Bonding Distance distribution of different charge states averaged over time and replicas, normalized.

While positively charged states have less n_{HB} , some of their bonds on average are shorter compared to neg and neut states, indicating different bond strengths[48]. When we analyze the distance distribution hydrogen bonding done by porphyrin axle, porphyrin core and CB6 separately, we see that protonated axle nitrogens for positively charged states are doing the shorter hydrogen bonds. While hydrogen bonds between bare nitrogens and water hydrogens are stronger as oxygen has higher electronegativity(~ 3.5), they seem to be longer compared to the bonds between water oxygens and nitrogen hydrogens. Our simulations demonstrate that charge state and the equilibrium location of CB6 rings greatly affect the hydrogen bonding.

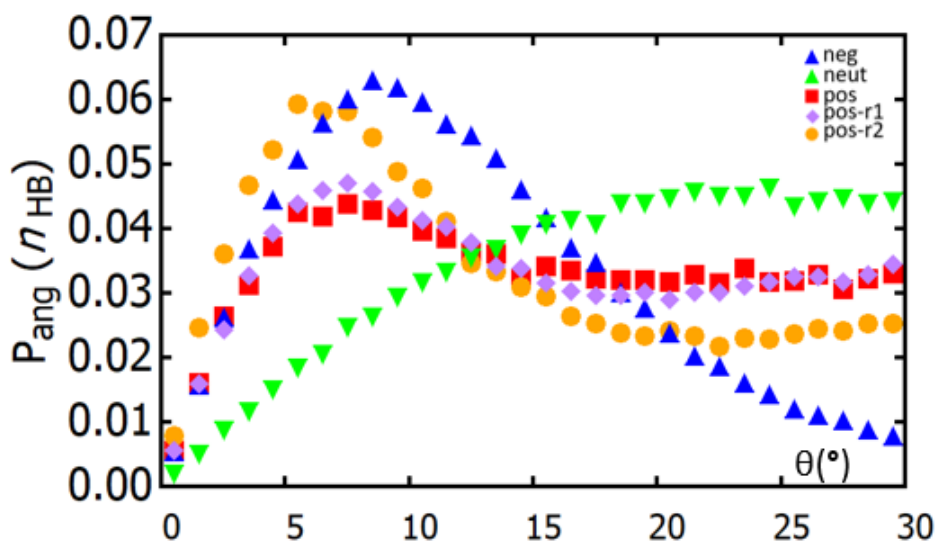


FIGURE 3.9: Hydrogen Bonding Angle distribution of different charge states averaged over time and replicas, normalized. All but neut state are identical.

Hydrogen bond angle distribution of different charge states does not vary greatly except for neut state. Neutral nitrogen terminals of neut state as observed only tend to do higher angle $\theta \sim 23^\circ$ hydrogen bonds with water. Overall, based on our simulations, we conclude that molecular conformation and interaction properties of [5]rotaxane is altered significantly by the protonation of axle nitrogens. While in angle distribution measurements neut state is distinctive, we do not see this singular characteristic in distance measurements.

3.1.3 Effect of Charged Porphyrin Core on the Structure

As stated before, the porphyrin core being a causative agent in properties of [5]Rotaxane such as solubility, the effect of positive charge on porphyrin core on the whole molecule is examined separately. The effect of protonation of the porphyrin core nitrogen on the molecular conformation is examined via extracting the positive core hydrogen from pos state (Fig.3.10) as the protonization pH of pos state and mid nitrogen are correspondent. Although the obtained structure is chemically improbable, it demonstrates drastic changes on the final simulated structure.

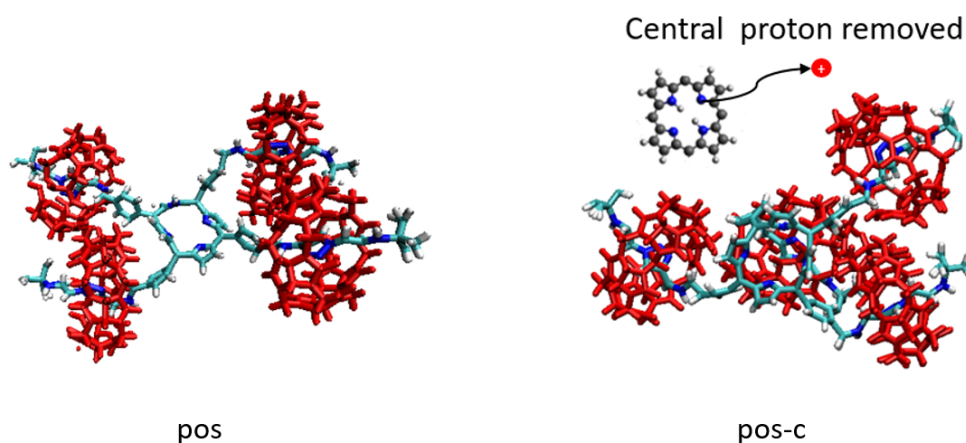


FIGURE 3.10: Final structures of 10ns simulations. Central proton removed pos state is labeled as pos-c conformation(right).

The average molecular conformation without a protonated core is similar to the collapsed configurations that we observe for the neg and neut states (Fig.3.2); in this configuration, CB6 rings collapsed around the porphyrin core.

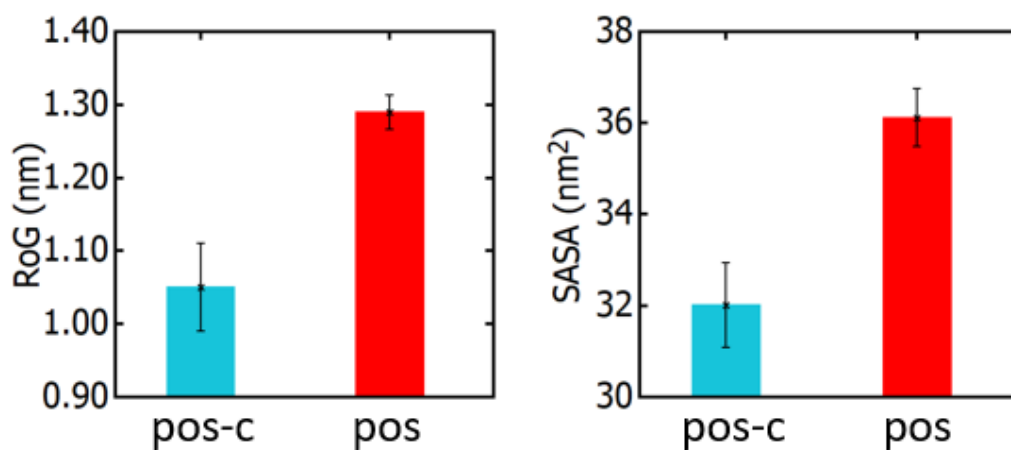


FIGURE 3.11: Average RoG and SASA values of central proton removed pos-c state compared to pos state.

Interestingly, the positional fluctuations of the axle parts also are more dramatics as compared to pos state, resulting in a higher standard error on R_g and SASA values. A distinction from positively charged states(pos, pos-r1, pos-r2) is the interaction between CB6 residues; while our neut and neg states have all CB6 groups closely packed at the center, for the pos-c state, at a given

time only two opposing CB6 groups interact, resulting in an asymmetrical shape (Fig. 3.10). In order to verify that the central interacting CB6 rings are not exclusive (i.e. same CB6 residues interact in all replicas), this simulation is replicated 10 times with different initial velocity values. 4 of 10 replicas had one pair of CB6 rings interacting while the rest 6 replicas had the other pair. Also given enough time ($\sim 10ns$) the central interacting CB6 pair may switch to the other pair.

3.2 Kinetics Studies of [5]Rotaxane Shuttling

In the previous section, we show that position of CB6 rings and resulting molecular conformations of [5]rotaxane is highly dependent on the charge state. We next ask the question how fast the [5]rotaxane can switch from one conformation to another upon a stimulus that can alter the charge state of the molecule. In order to achieve this, we assigned the equilibrium conformation of a charge state as the initial configurations of another set of simulations but with a new charge state (e.g., neg \rightarrow pos, etc.). In this way, we were able to observe effects of rapid charge alterations on the time-dependent transitions of the molecular configurations. We mainly investigate the kinetics of transitions, pos \rightarrow neut-p and pos \rightarrow pos-r1. In the case of pos \rightarrow neut-p case, it was reported that the center most hydrogens of the axle that are adjacent to benzyl groups are first to deprotonate with increasing pH, thus the porphyrin has a transition state named neut-p (Fig.3.1) here that has partially protonated axle hydrogens [17]. We approach the analysis both of these transition in the same manner, firstly by visual inspection, then by simply calculating the solvent accesible surface area change with time as we see that it is directly correlated with the axial locations of CB6. For both cases we measure the transition both ways as for the pos \leftrightarrow pos-r1 the macrocycle shuttling might act irreversibly with constant temperature.

3.2.1 POS \leftrightarrow POS-R

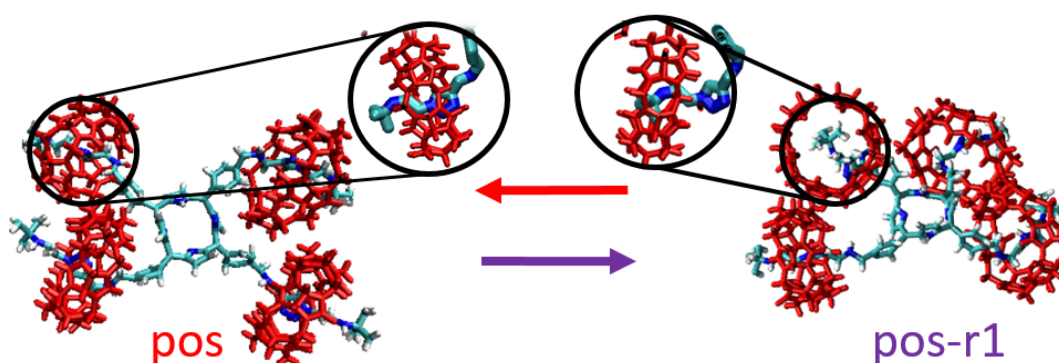


FIGURE 3.12: CB6 transition along axle in pos \leftrightarrow pos-r1 state change simulations. 2 of 4 rings randomly shuttle outwards along the axle with forward(purple) direction, only one of the shuttled CB6 shuttle back for backward(red) direction.

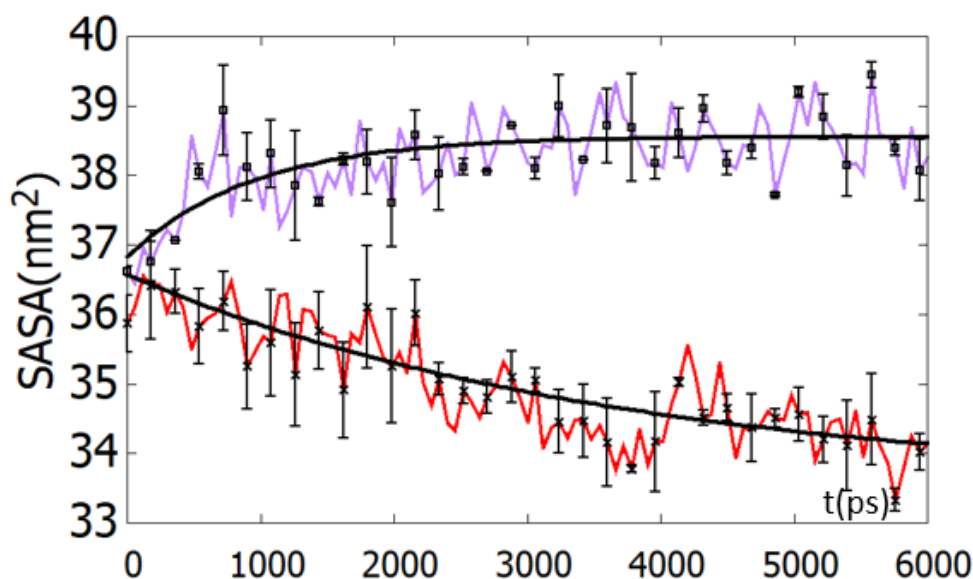


FIGURE 3.13: Solvent accessible surface area versus time data of both ways of transition($\text{pos} \rightleftharpoons \text{pos-r1}$). Red line denotes $\text{pos-r1} \rightarrow \text{pos}$ transition, purple line denotes $\text{pos} \rightarrow \text{pos-r1}$ transition.

In general, the transitions between states with similar molecular conformations (e.g., neg and neut) did not show any significant time-dependent configurational changes when SASA and hydrogen bonding were monitored. However, we observed the most drastic changes in the configurational properties of [5]rotaxane in the cases, in which the pos-r1 state is the final state and *vice versa*. Almost in all of those transitions, time-dependent configurational were accompanied by simultaneous shuttling motion of more than one CB6 rings along the axles (Fig. 3.12).

In this transition, shuttling response of CB6 rings are not all-in-once; while some CB6 move away from the porphyrin core, some CB6 rings stay on the protonated triazole groups. The shuttling of CB6 rings along the axles can also manifest itself as apparent alterations in inter and intra-molecular interactions. Hence, we quantified time-scales of shuttling motion by monitoring time traces of hydrogen bonding between [5]rotaxane and water as well as that of SASA profiles. Averaging over > 20 simulation replicas revealed that SASA increase rapidly upon the alteration of the charge state (i.e., from pos to pos-r1) (Fig. 3.13) before reaching a saturation value of 38.5, close to the SASA value of state pos-r1 while n_{HB} responds rather weakly (5%). By fitting simple exponential functions, $f(t) = 1 - \exp(-t/\tau)$ to SASA data of

pos \rightarrow pos-r1 shuttling, we obtain characteristics shuttling times of around $\tau_{SASA} = 934.9 \pm 10$ ps. As for the other way pos-r1 \rightarrow pos, the SASA decreases even below the SASA value of state pos(Fig.3.6). Fitting again the simple exponential functions, $g(t) = 1 + \exp(-t/\tau)$, we obtain the shuttling time around $\tau_{SASA} = 3697.9 \pm 15$ ps. Upon close inspection of the configurations of individual replicas of both ways simulations, the reason behind this asymmetry appears as backwards shuttling of CB6 rings being slower and partial for all cases. For all 20 replicas of pos-r1 \rightarrow pos simulations with 300K temperature, one of the shuttled CB6 rings relocate back onto the triazole group while the other one stays on the outer amine group, resulting in a partially stabilized pos state, which in turn explains the decrease of SASA value below the equilibrium pos state, as the CB6 located on the tip of the axle bends the axle towards core porphyrin, lowering the SASA further. This suggests that while protonization on its own is enough of a factor for forward shuttling, additional interference such as heat is required to restore the system to its initial pos state.

3.2.2 POS \leftrightarrow NEUT-P

Continuing with neut-p \rightarrow pos transition, we do not see any shuttling behavior as from pos to neut-p state, the molecule collapses to its center rapidly, forming a shape completely identical with the neut state.

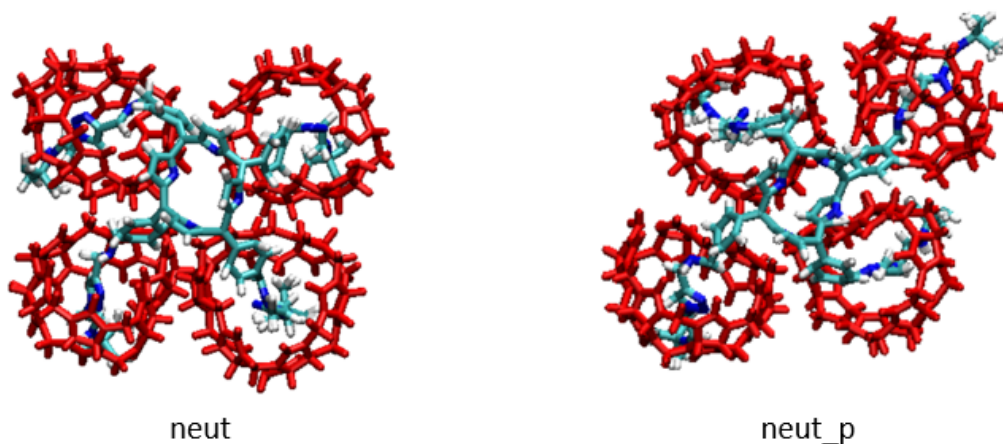


FIGURE 3.14: Final equilibrium conformation of pos \rightarrow neut-p transition obtained after 5ns and neut state.

Thus the expected noticeable shuttling to the deprotonated central nitrogen is not observed as the rapid axle bending towards the core, prevents the CB6 mobility. Upon close visual inspection, we see that CB6 ever so slightly move towards core before the axle bending. Reverse direction(neut-p \rightarrow pos) does not exhibit any interesting properties as the folded axles extend with no CB6 movement, reverting back to the equilibrium pos conformation (Fig.3.2).

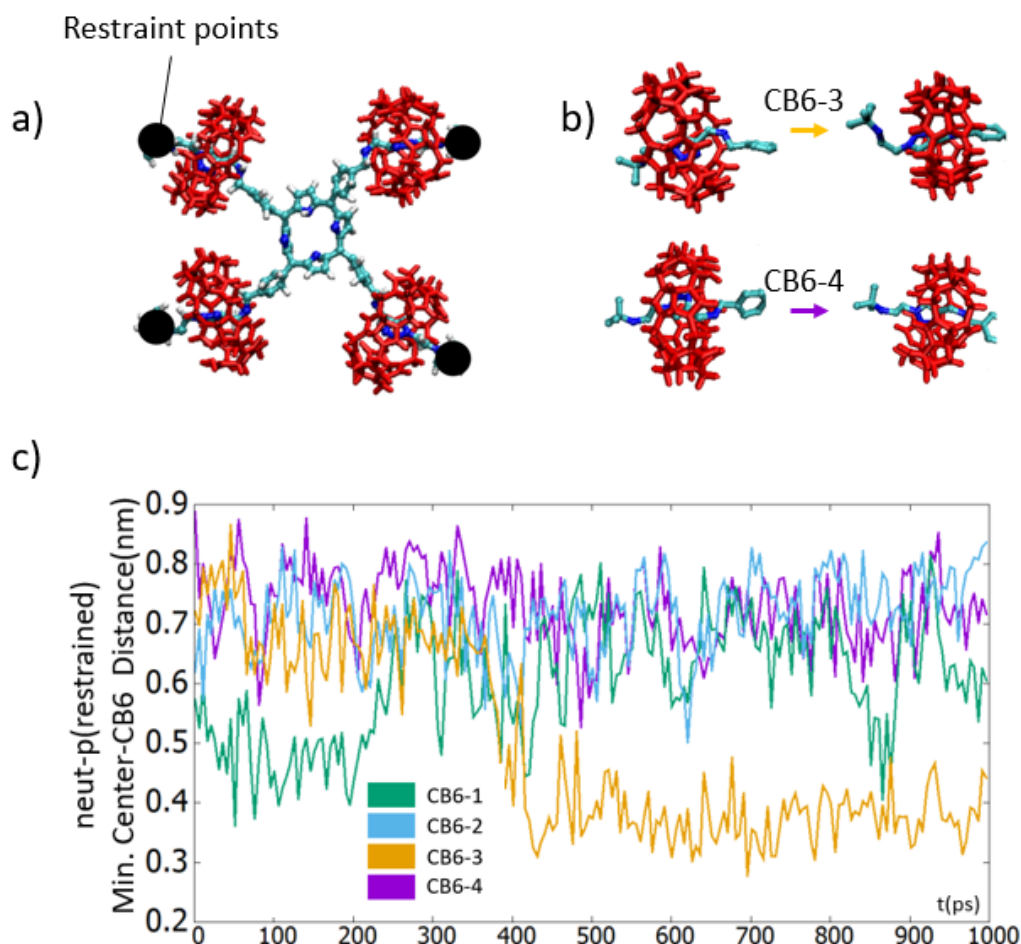


FIGURE 3.15: Restraint points of neut-p structure(a), the inwards shuttling of CB6 rings captured from different times(b) and minimum distance between porphyrin core and CB6 (c) versus time.

To isolate the CB6 movement of pos \rightarrow neut-p transition, we apply external constraints to the outermost carbons (Fig.3.15a) [5]rotaxane to keep the conformation on a spread state. With this approach, we are able to observe the movements of CB6 towards the core. As we expected from the experiments, restrained neut-p model exhibits increased CB6 mobility, and all CB6 rings

are able to move freely on the axle towards the porphyrin core at different times. The shuttled CB6 does not necessarily stay at the inner amine groups as the triazole is still a preferable stable site.

Overall, our simulations suggest that [5]rotaxane can respond to changes in the charge states quite rapidly by allowing shuttling of CB6 rings along the axles both inwards and outwards while demonstrating a one way controllable switch property.

3.2.3 Essential Dynamics Analysis

It was previously demonstrated that the neut state of [5]Rotaxane is also subject to the CB6 shuttling behavior from triazole to inner axle locations. While we have not observed this behavior on state simulations, the collapsed conformation of the neut state was rather curious in the sense that it could prevent CB6 shuttling via rapid interaction of axles. To address this, we have restrained the position of furthestmost atoms of axles with the same constraint that are applied to the neut-p state, then proceeded with the simulations. In order to probe finer details of the CB6 movement on the axles, we have employed principle component analysis on the covariance matrix of CB6 rings' positions along the simulation. Averaging over the projection of largest eigenvectors that does not correspond to global movement gave us a good isolation of spatiotemporal CB6 behavior. Here "large" or "high" eigenvector refers to the eigenvectors with the highest eigenvalues. We mainly did this analysis for pos-r1 state as it shows outwards shuttling and restrained neut state to investigate if the non protonated axle provides mobility for CB6.

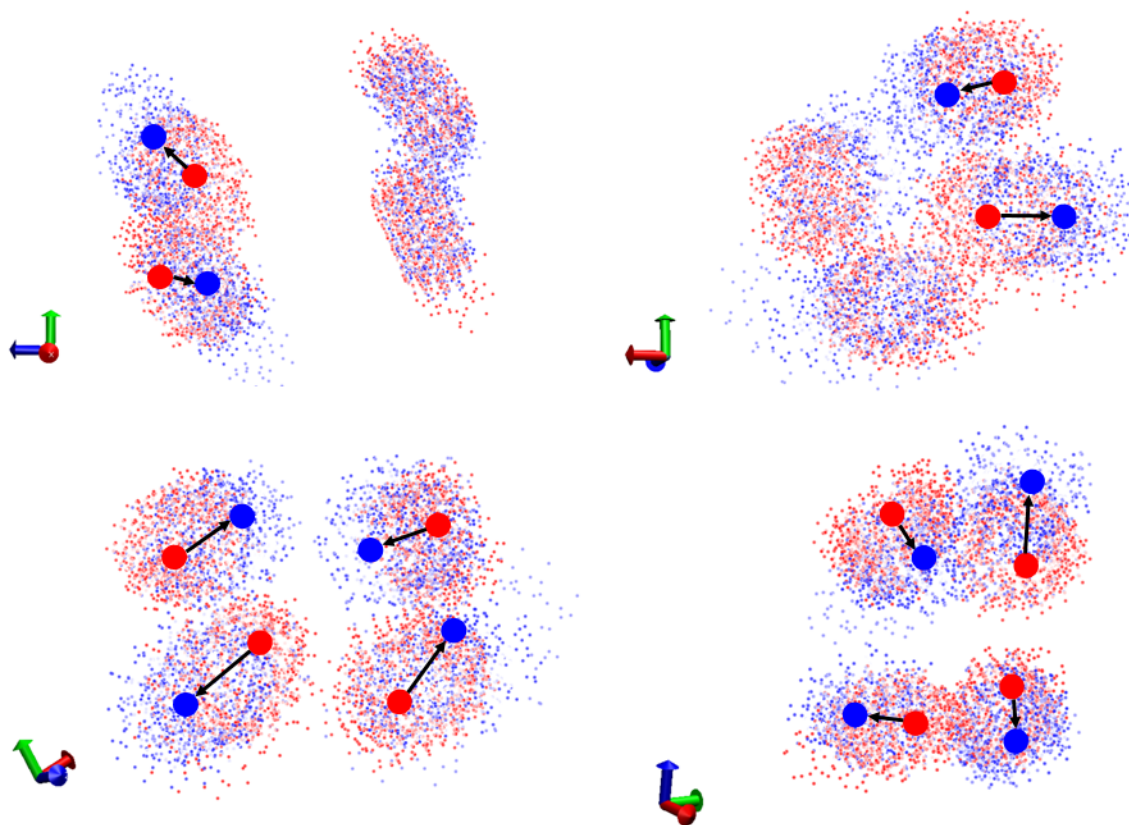


FIGURE 3.16: High eigenvector trajectory of CB6 rings of **pos-r1** state. Colored from starting time frame, red dots to final time frame blue dots denote average positions of CB6 atoms. Blue and Red circles are on the center of high density red and blue points.

The axle and asymmetric drift movements of CB6 complexes of [5]Rotaxane is extracted from pos-r1 time trajectory via previously defined essential dynamics analysis methods. Here we see (Fig. 3.16) that high eigenvectors of covariance matrix projection of non weighted CB6 atoms correspond to axial rotation from the center porphyrin. As axles of porphyrin flail around the atom, CB6 also move sideways with the axles. The blue and red circles show both shuttling and axle bending movements (Fig. 3.16).

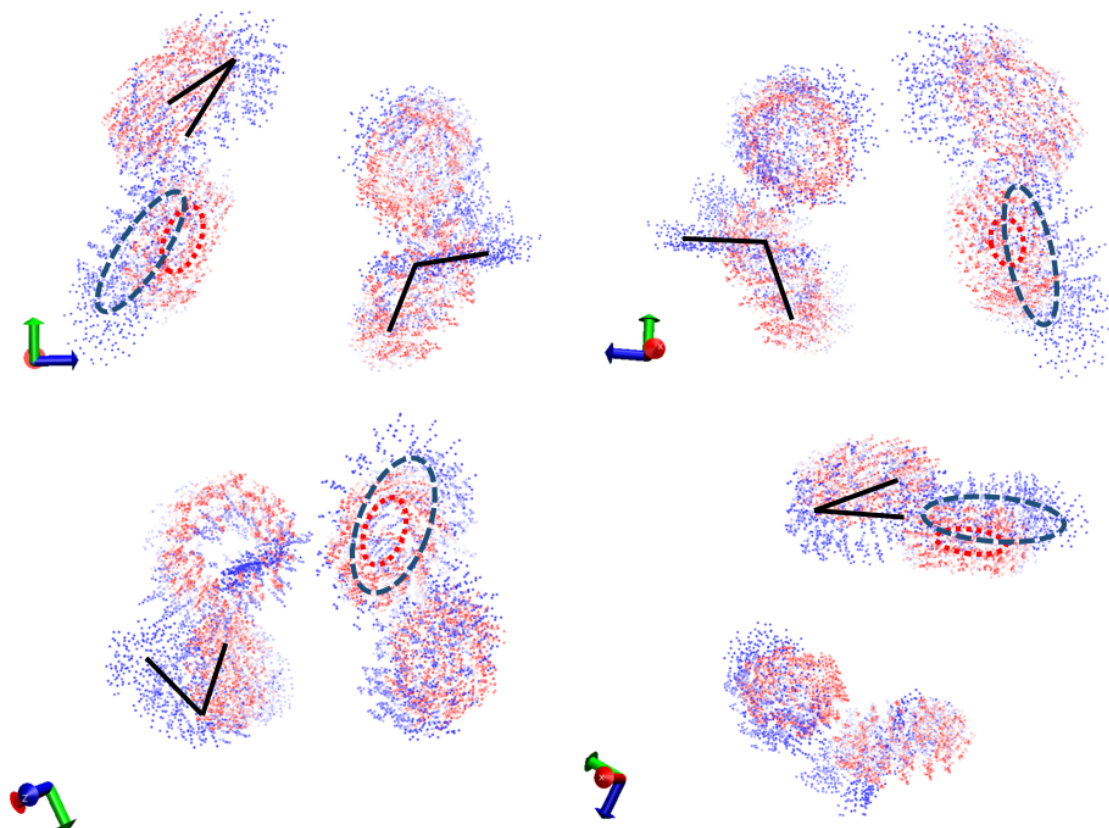


FIGURE 3.17: Low eigenvector trajectory of CB6 rings of **pos-r1** state. Colored from starting time frame positions (red dots) to final time frame positions (blue dots) denote average positions of CB6 atoms. Since for low eigenvectors axial global movements are not present CB6 rotations are shown by angles with black lines and CB6 expanding/shrinking are shown by dotted circles.

Other than relatively large scale movements, CB6 molecules also shrink expand and rotate around the axle. These minor movements are given in Fig. 3.17. Unlike shuttling, axial bending and drift, these small movements do not shift the center of CB6 rings greatly.

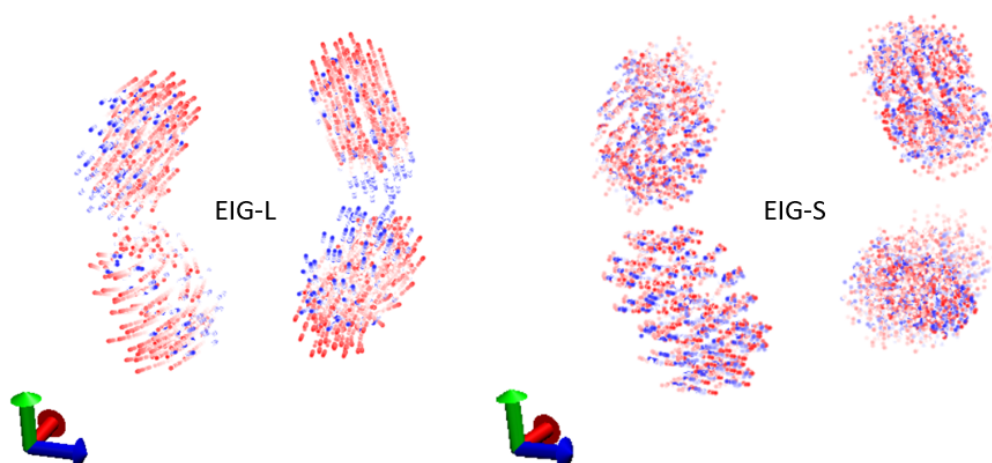


FIGURE 3.18: Eigenvector trajectory of CB6 rings of **restrained neut** state. Colored from starting time frame positions (red dots) to final time frame positions (blue dots) denote average positions of CB6 atoms.

Unlike pos-r1, restrained neut state atoms are much more stationary as they are both restrained and there is no shuttling. As there is no global movement, there is not much difference in high and low eigenvector based models.

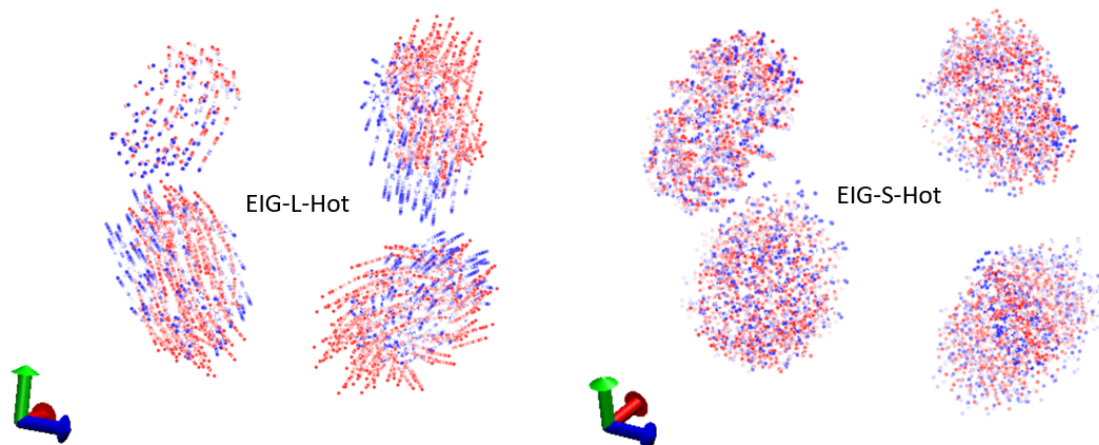


FIGURE 3.19: Eigenvector trajectory of CB6 rings of **restrained neut** state simulated at 350K. Colored from starting time frame positions (red dots) to final time frame positions (blue dots) denote average positions of CB6 atoms.

Increasing the temperature of restrained neut state result in a discrepancy between low and high eigenvalue models. In this higher kinetic energy state we see slight global CB6 movements along the axle. While still there is no shuttling to inner or outer amine groups, the center of CB6 rings fluctuate much more between triazole groups' centermost and outer parts. This suggests that triazole sites are not as stable as other states for CB6 to stay on for neut state [5]Rotaxane.

In the light of all our simulations and analysis, we can predict solvent interaction and conformation effects that should be observed experimentally. Following from the charge state simulations corresponding to different pH values, we see that high acidic solutions of low pH causes the [5]Rotaxane to collapse which in turn should alter the self assembly properties. As we show in the visual trajectory of neut state, CB6 interact with each other as well as the porphyrin core, thus we expect multiple [5]Rotaxane interact from CB6 to form closely packed circular structures. Although our neut state simulations are not in concordance with the experimental predictions of CB6 shuttling onto the benzyl cite and staying there, we can pinpoint the exact frame destabilization of the each CB6 ring from triazole cites via our essential dynamics analysis on restrained neut state. We also show that, axle benzylamine group deprotonation mobilizes the CB6 as we see in restrained neut-p simulations. The simulation results support the existence of a tuneable mechanically interlocked molecular structure that responds to pH and temperature changes. The transitions and their inclination to occur can be summarized as the following:

- **neg(exotic) ↔ neut, neut ↔ neut-p,neut-p ↔ pos-c:** Only pH change is enough to achieve these equilibrium structures. No shuttling is observed as the axle are closely interacting.
- **pos → pos-c:** Molecule collapses rapidly via two interacting opposite axles, effectively reducing SASA and RoG.
- **pos → neut-p:** Molecule collapses rapidly (~ 100 ps), achieving the closed neut-p structure without shuttling.
- **pos → restrained neut-p:** The CB6 move along the axle freely shuttling to inner CB6 and triazole.
- **pos → restrained neut:** The CB6 move along the axle freely but not pronounced as pos → restrained neut-p shuttling to inner CB6 and triazole.

- **pos** → **pos-r1**: Two opposite CB6 shuttle to the outer amine group within 1 ns.
- **pos-r1** → **pos**: One of the shuttled CB6 shuttle back towards the triazole within 3 ns. Equilibrium pos structure is not recovered suggesting the need of additional stimuli.
- **pos** → **pos-r2(exotic)**: All CB6 shuttle towards core.

3.3 Poly Rotaxane and Poly-[5]Rotaxane Network

A previous experimental study demonstrate that [5]rotaxane can localize at a water-chloroform interface, this localization leads to the formation of a 2d network of [5]rotaxane molecules [20]. To investigate the effect of charge state on such network structures, we constructed poly-rotaxane structures by introducing covalent bonds between the terminal groups of the axle parts of [5]Rotaxane to obtain both periodic and 2×2 discrete macromolecular structures, which will be referred as Poly Rotaxane(PR) and Poly Rotaxane Network(PN) respectively. The non periodically bonded 2×2 PR molecule is simulated in-water(NPT) and on-water(water-void interface NVT).

3.3.1 PR Simulations

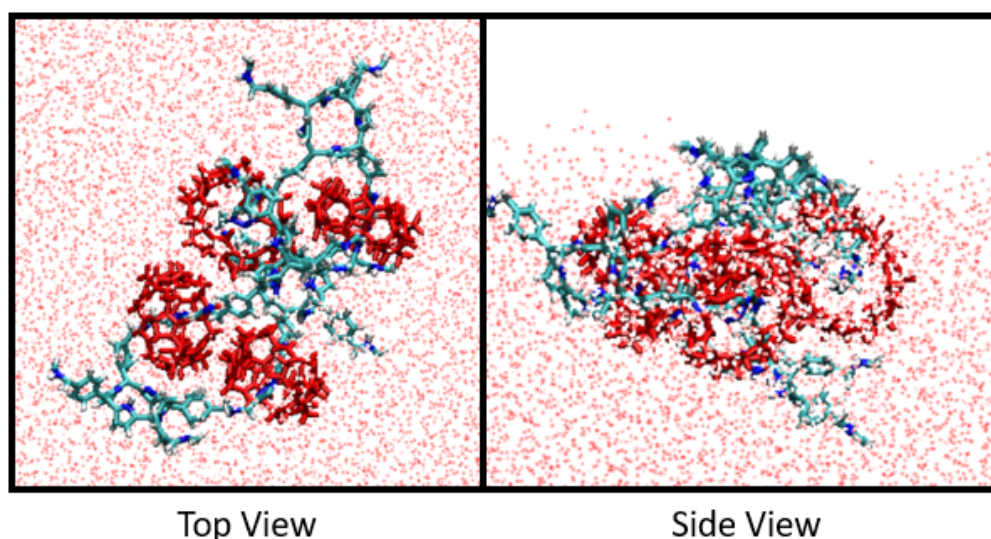


FIGURE 3.20: 2×2 polyrotaxane on water surface at 300K(NVT).

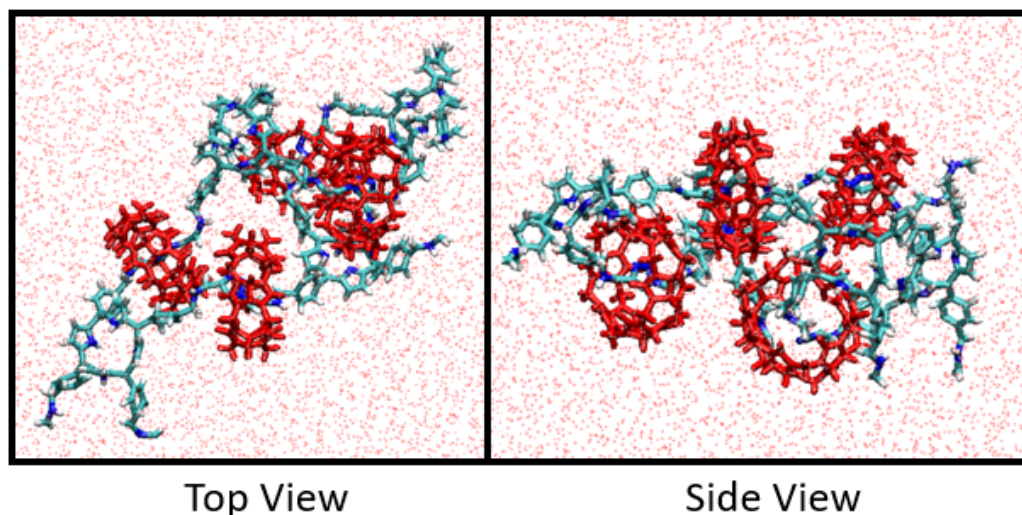


FIGURE 3.21: 2×2 polyrotaxane in water at 300K(NPT).

2×2 PR structures constructed from 4 pos state [5]Rotaxane molecules exhibit similar properties when simulated both in water and on water conformations. From visual inspection, it is seen that CB6 rings are attracted to each other, affecting the final shape of the 2×2 poly rotaxane molecule. After initial local movements, the structure preserves its shape drifting along the water surface without flipping or rotating. Calculating the energy of interaction for in-water and on-water cases show that the encapsulation by water molecules does not affect the interactions between CB6 significantly.

	LJ	LJ(SR)	COUL	COUL(SR)
IN	-325	-758	-9192	3421
ON	-308	-798	-9212	3430

TABLE 3.2: Intramolecular interaction energy in terms of KJ/mol of CB6 rings on two systems. IN-In water, ON-On air water interface. LJ-Lennard Jones, COUL-Coulomb, SR-Short Range

3.3.2 PN Simulations

Moving on with the periodic bonds applied to 2×2 polyrotaxane molecule, our simulations shows that poly-rotaxane macromolecular 2d networks can maintain their configuration stably at the interface of chlorophyl and water as also demonstrated experimentally, owing to the highly amphiphilic nature of [5]rotaxane. We utilize water and chloroform molecules to form create a surface to put PN on, as it was shown by Donus et al. that in this interface PN structure is both produced and stable.

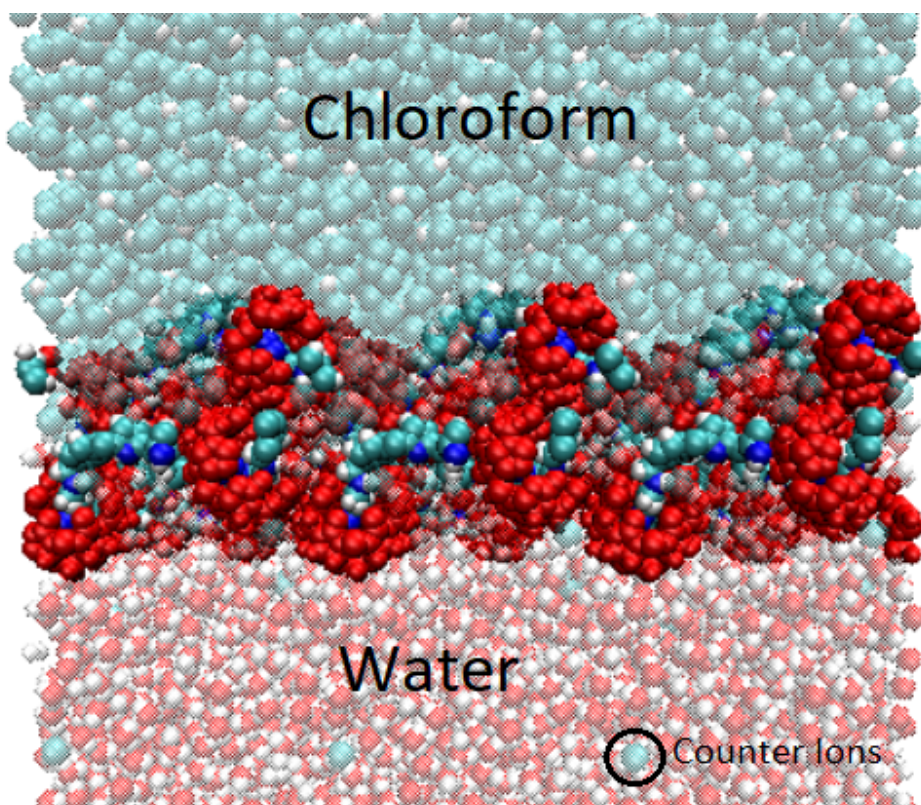


FIGURE 3.22: Side view - final simulation time frame PN structure. Transparent vdW models are water(red) and chloroform(blue). The counter ions are added via water substitution and as expected are mainly close to the interface.

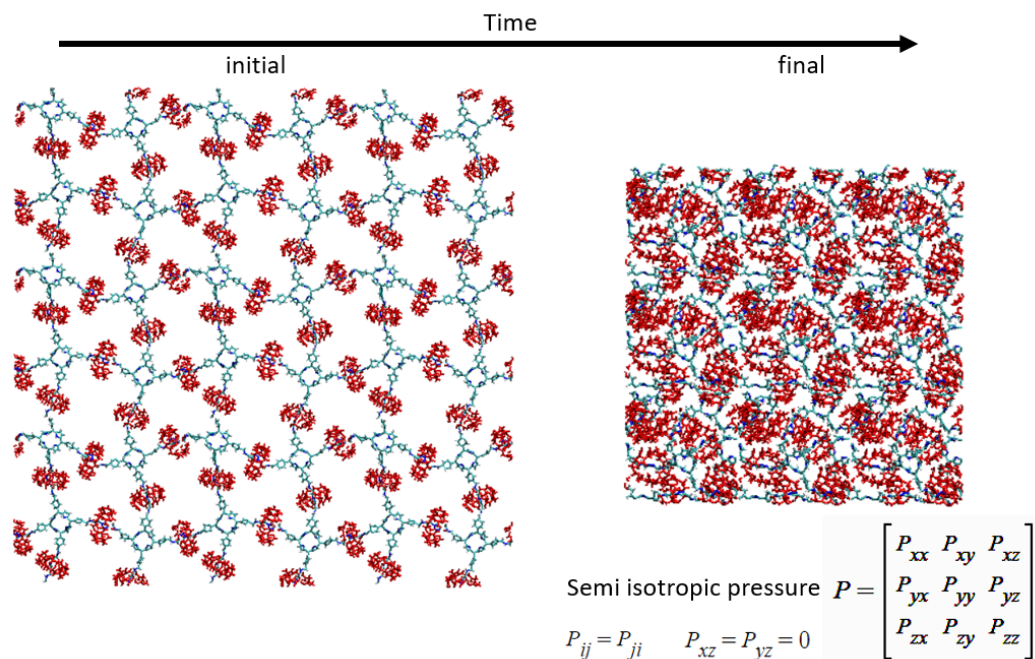


FIGURE 3.23: Polyrotaxane network in water, chloroform interface.(NPT) Semi-isotropic pressure coupling is used with given pressure matrix equalities. The initial conformation(left) and final conformation(right)

Visual inspection reveals that the porphyrin groups are closer to chloroform phase while CB6 rings are mostly immersed in water phase which was also the case for water surface PR molecule. At the interface, a well-preserved network structure, in which poly-rotaxanes are of a planar configuration, can persist throughout the duration of the simulations. Notably, a single PR molecule immersed in water or air-water interface is settled on a collapsed state, suggesting the requirement of a large scale assembly of poly-rotaxanes at the interface to obtain such 2d networks. As the structure shape changes with time, the structure deforms into its final surface area conformation rather quickly ~ 500 ps and preserves its shape and size throughout the 20 ns simulations.

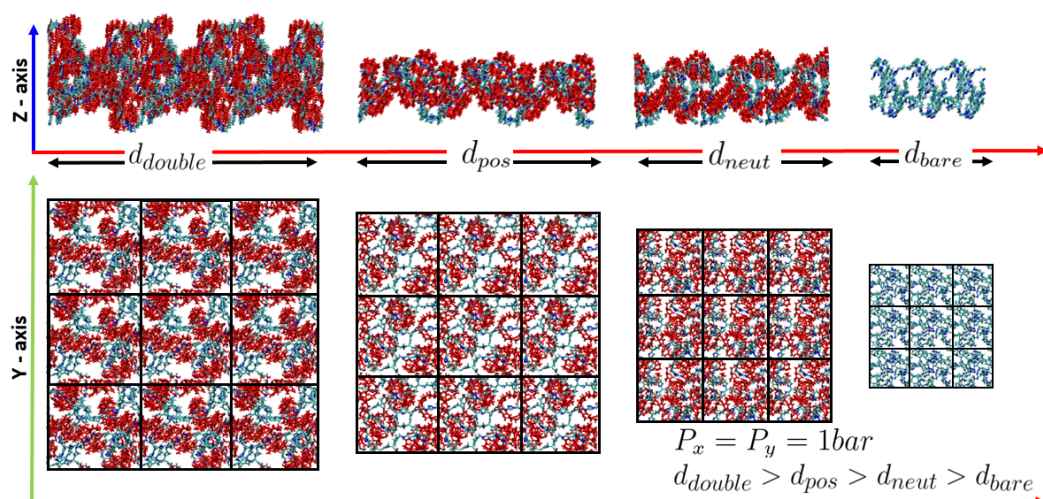


FIGURE 3.24: Polyrotaxane network charge states in water-chloroform interface(NPT). From left to right, double layer positive PN, positive PN, neutral PN and CB6 absent PN. d_{neut} is the length of x and y axis in the end of $5ns$ md simulations.

PN system substructure interact rapidly, achieving the final 'squeezed' state in $\sim 2ns$. As expected from the simulations of [5]rotaxane structure charge states (Fig.3.25), the neutrally charged PN has much less surface area collapsing under the 1 bar pressure Fig.3.25. Although being a toy model, to show the effect of CB6 residues, on the surface area and in turn porosity, CB6 absent model named bare is also simulated and as expected it collapses completely under 1 bar of pressure. In a subset of simulations, we removed the CB6 rings from the structure. These simulations lead to a highly collapsed 2d network structures, suggesting the role of CB6 rings in the extended 2d network configuration. Supporting the surface formation properties, the bi-layer state that has dimensions d_{double} has the highest surface area and we expect this trend to continue with the number of layers. Utilizing a numerical zeolite model porosity calculation library provided by T.F. Willems et al. we measure the metric called largest free void sphere diameter that is related to porosity[56]. Largest free void sphere diameter simply gives the radius of the largest sphere that can pass through our molecular structure.

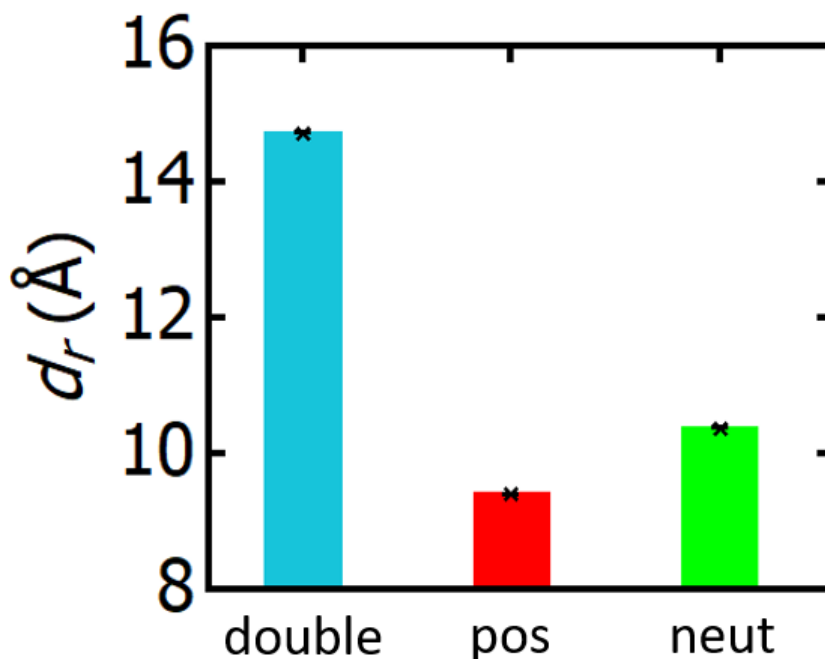


FIGURE 3.25: Final largest void free sphere radii of three PN structures.

We observe that although neutrally charged PN has less surface area, it has slightly larger cavity compared to positively charged PN structures. Correlated with the experimental findings, double layer PN structure has both larger surface area and cavities. This suggests that two layers interacting with each other prevents collapsing and reinforces the network structure providing higher resistance to planar pressure.

Chapter 4

Conclusion

In this work higher order [5]Rotaxane molecule and its network derivatives are simulated with atomistic MD simulations. pH dependent shuttling behavior of 5-Rotaxane and its network derivative PN is investigated via equilibrating different initial protonation systems.

[5]Rotaxane is a significant MIM because, porphyrin core of [5]Rotaxane has cytotoxic behaviour via generation of reactive oxygen species and can be utilized as a kill switch if one finds a mechanism to control the toxicity. It was also demonstrated in recent experiments that CB6 molecule is a possible candidate to equip onto porphyrin to regulate this cytotoxicity with light excitation. This shuttling motion is analyzed experimentally via NMR and UV-Vis spectroscopy with an appropriate chromophore. With these MD simulations we now have an atomic description of the Newtonian model of [5]Rotaxane molecule.

With this classical model, we are able to demonstrate and quantify the pH dependent shuttling rates and spatio-temporal details of this mechanism. We predict an asymmetrical switch property that is present in many rotaxane derivatives. We see in our simulations that the location of CB6 rings and conformation of [5]Rotaxane molecule is tunable with protonization. We also show the stabilization effect of central nitrogen protonation of porphyrin core. For further research paths, the large conformational distinction between neut and pos state can be investigated since the interaction of multimolecular neut and pos state [5]Rotaxane systems could exhibit different interaction behavior.

For PN simulations, we were able to predict the necessity of positive charge on preserving the high surface area of the network throughout the semi isotropic NPT simulations. While the bare model of PN without CB6 rings is unobtainable experimentally, it shows the effect of CB6 rings on surface formation properties as without CB6 the lateral pressure collapses the system. As the neut state PN system has less surface area, pH of the medium of PN formation can be utilized to obtain desired surface properties. Overall our findings from these computational results are fully concordant with experimental observations and we believe that we provide additional insight into the pH based applications of this light activated toxic agent.

The major limitation of the classical MD simulations is the constant nature of the point charges that does not change depending on the structure. This is even a greater limitation for simulating MIMs as the mechanically bonded molecules are in close enough proximity to alter whole electronic structure. In this work we used the approach of not distributing net charges along the structure to minimize the spatial errors that can alter the simulation results. Further research on this molecule or for other MIMs could be directed on understanding the charge distribution changes depending on the molecular conformation and macro cycle locations, utilizing quantum interaction methodology.

Appendix A

Essential Dynamics Figures

Root mean square fluctuations(RMSF) of atoms positions in the neut and posr-1 systems are given below. We expect the low eigenvectors RMSF of covariance matrix of the pos-r1 simulation trajectory to correspond to local movements such as CB6 shuttling, thus only the indexes of CB6 atoms(210-650) should have high spikes in the graphs. And for the restrained neut state, since the porphyrin axle's furthestmost groups are immobilized, all eigenvectors only contribute to local movements.

A.1 NEUT - Restrained

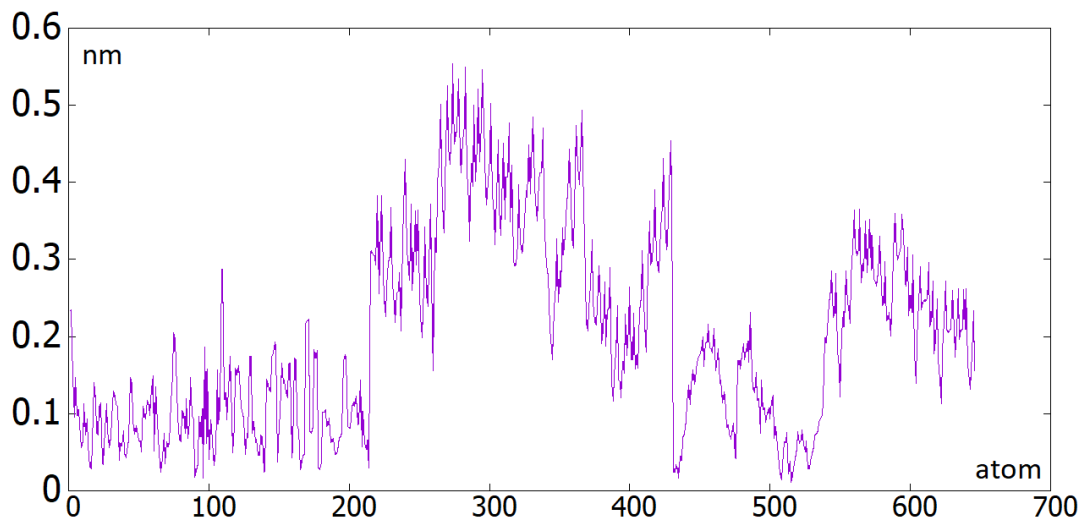


FIGURE A.1: Highest Eigenvector Projected RMSF - Neut System - 300K Temperature

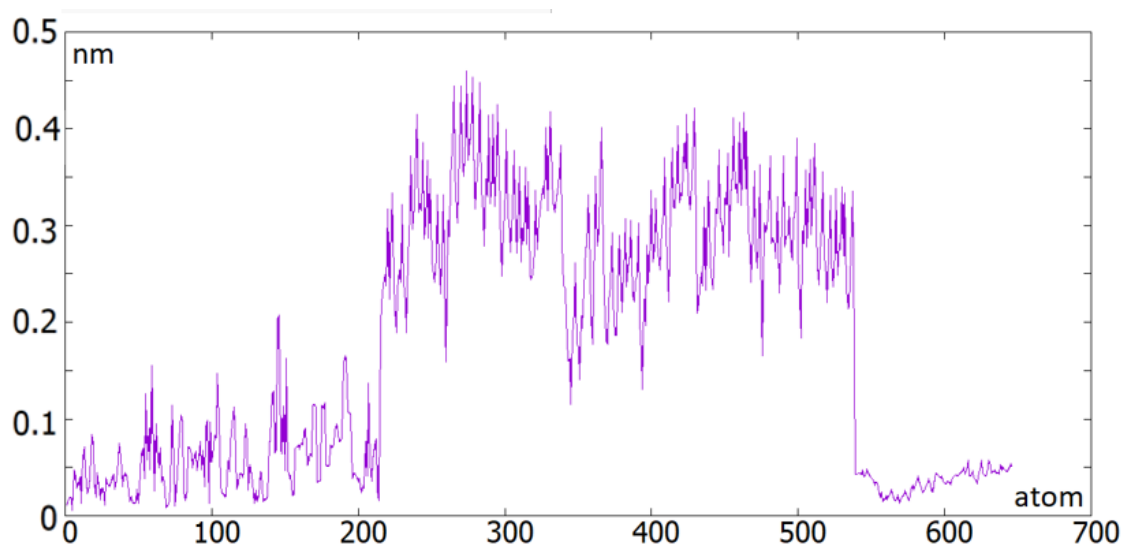


FIGURE A.2: High Eigenvectors Projected RMSF - neut system
- 350K Temperature

Atom indices from 210 to 650 are atoms of CB6 residues and as we see they give the peaks in the RMSF calculations.

A.2 POS-R1

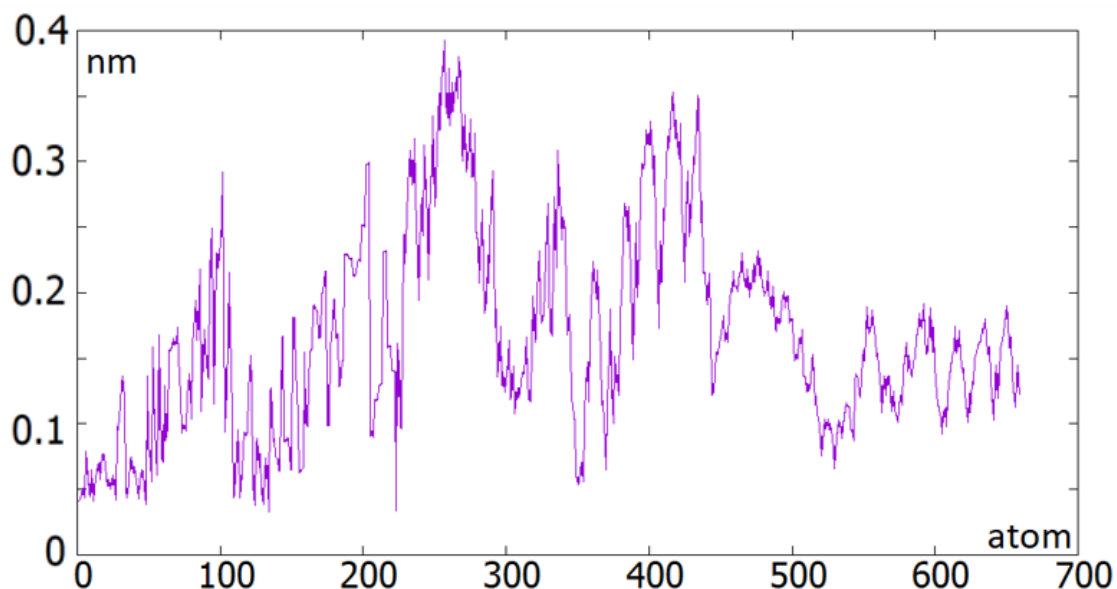


FIGURE A.3: High Eigenvectors Projected RMSF - posr-1 sys-
tem - 300K Temperature

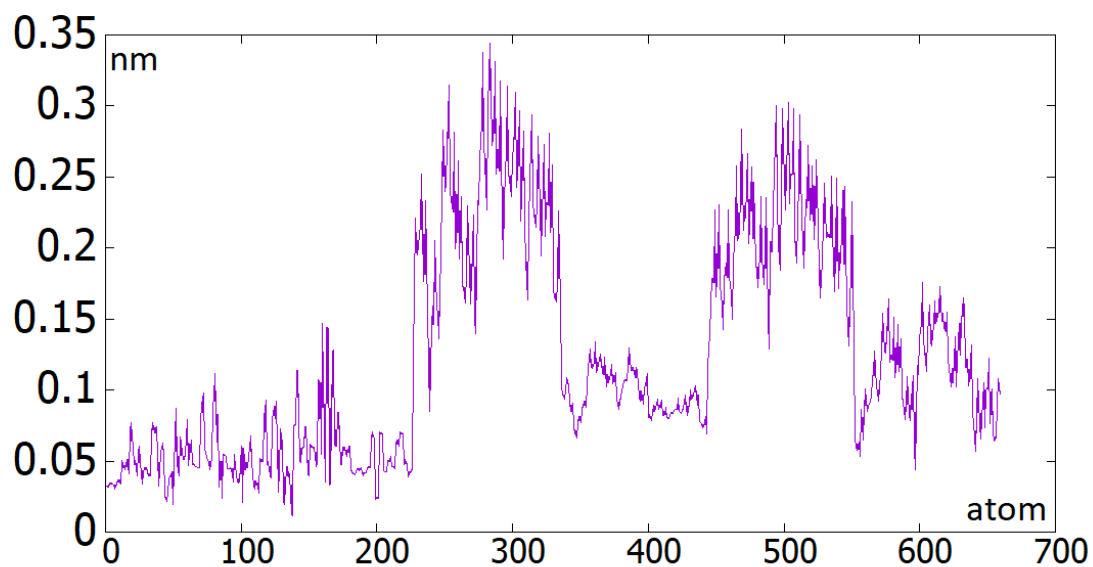


FIGURE A.4: Low Eigenvectors Projected RMSF - posr-1 system
- 300K Temperature

Low eigenvector RMSF reveals the highest contributing atoms to be two of the CB6 rings that correspond to the peaks (Fig.A.4.)

Appendix B

Cumbersome Details of Simulations

In order to initialize and simulate a system of molecules in any classical molecular dynamics software, there are some concrete steps. The most obvious step is acquiring the simulation data of atom positions, interaction parameters, charges and atom types. Since we are excluding all the quantum interactions that does not have a classical counterpart(i.e. electron exchange correlation), we deviate from the realistic results if we treat every atom individually. This means that the intrinsic properties of a hydrogen that is bonded with an oxygen should not be treated same with another hydrogen that is bonded to a carbon. Thus we utilize force fields that have specific parameters for specific atom types. In our case a C-H bond hydrogen is referred as "HC" while N-H bond hydrogen is referred as "H".

The porphyrin molecule's atoms are first given identifiers relating to the corresponding GROMOS force field simply by classification of bonds they are doing. Thankfully the structure data containing atomic positions is rather easy to obtain from online molecule databases. If the molecule structure is not readily available, one might need to assemble it as a text file with certain tools(Avogadro, Chem3D). Gromacs utilizes two files to hold all the data. The position/structure file (.pdb/.gro extensions) that holds no information about any interaction and the topology file(.top extension) that holds every required information except the positions. These data definitions are present in all MD models and unlike quantum calculations that characterize the bonds with only spatial and intrinsic properties of atoms, in MD all interaction parameters must be supplied from outside.

Once all the parameters of the system's atoms are gathered and the initial simulation model is generated, the simulation parameters and coupling methods should be decided. These are discussed in depth in Chapter 2.

After running the simulations, information should be extracted from the simulation data. For the GROMACS program, as the simulation output are written in a non readable format, analysis scripts are utilized. The analysis part changes greatly depending on the simulation software. The SASA and RoG calculations of GROMACS scripts utilize a well researched algorithm, thus are fast and easy to implement. The output data for GROMACS is written as a trajectory(.xtc, .trr extensions) file, structure file and an energy(.edr extension) file. Additional scripts to handle the extracted data is written by hand in this work which simply reads the data from different text files and does the operations.

Bibliography

- [1] David P. Rotella. "The Critical Role of Organic Chemistry in Drug Discovery". In: *ACS Chemical Neuroscience* 7.10 (2016). PMID: 27623164, pp. 1315–1316. DOI: [10.1021/acschemneuro.6b00280](https://doi.org/10.1021/acschemneuro.6b00280). eprint: <https://doi.org/10.1021/acschemneuro.6b00280>. URL: <https://doi.org/10.1021/acschemneuro.6b00280>.
- [2] Wesley R. Browne and Ben L. Feringa. "Making molecular machines work". In: *Nature Nanotechnology* 1.1 (2006), pp. 25–35. DOI: [10.1038/nnano.2006.45](https://doi.org/10.1038/nnano.2006.45).
- [3] Jonathan R. Nitschke. "The nature of the mechanical bond. from molecules to machines von Carson J. Bruns und J. Fraser Stoddart." In: *Angewandte Chemie* 129.1 (2016), pp. 39–39. DOI: [10.1002/ange.201611682](https://doi.org/10.1002/ange.201611682).
- [4] Kelly S. Chichak et al. "Molecular Borromean Rings". In: *Science* 304.5675 (2004), pp. 1308–1312. DOI: [10.1126/science.1096914](https://doi.org/10.1126/science.1096914). eprint: <https://www.science.org/doi/pdf/10.1126/science.1096914>. URL: <https://www.science.org/doi/abs/10.1126/science.1096914>.
- [5] Simon J. de Veer, Meng-Wei Kan, and David J. Craik. "Cyclotides: From Structure to Function". In: *Chemical Reviews* 119.24 (2019). PMID: 31829013, pp. 12375–12421. DOI: [10.1021/acs.chemrev.9b00402](https://doi.org/10.1021/acs.chemrev.9b00402). eprint: <https://doi.org/10.1021/acs.chemrev.9b00402>. URL: <https://doi.org/10.1021/acs.chemrev.9b00402>.
- [6] David A. Leigh, Vanesa Marcos, and Miriam R. Wilson. "Rotaxane Catalysts". In: *ACS Catalysis* 4.12 (2014), pp. 4490–4497. DOI: [10.1021/cs5013415](https://doi.org/10.1021/cs5013415). eprint: <https://doi.org/10.1021/cs5013415>. URL: <https://doi.org/10.1021/cs5013415>.
- [7] Gottfried Schill. *Catenanes, rotaxanes, and knots*. Vol. 22. Elsevier, 2017.
- [8] Bin Yao et al. "Recent Progress in Light-Driven Molecular Shuttles". In: *Frontiers in Chemistry* 9 (2022). ISSN: 2296-2646. DOI: [10.3389/fchem.2021.832735](https://doi.org/10.3389/fchem.2021.832735). URL: <https://www.frontiersin.org/article/10.3389/fchem.2021.832735>.

- [9] Maximilian Wolf et al. "Light triggers molecular shuttling in rotaxanes: Control over proximity and charge recombination". In: *Chemical Science* 10.13 (2019), pp. 3846–3853. DOI: [10.1039/c8sc05328f](https://doi.org/10.1039/c8sc05328f).
- [10] Kelong Zhu, Giorgio Baggi, and Stephen J. Loeb. "Ring-through-ring molecular shuttling in a saturated [3]Rotaxane". In: *Nature Chemistry* 10.6 (2018), pp. 625–630. DOI: [10.1038/s41557-018-0040-9](https://doi.org/10.1038/s41557-018-0040-9).
- [11] Dönüs Tuncel et al. "Molecular switch based on a cucurbit[6]Uril containing bistable [3]Rotaxane". In: *Chem. Commun.* 13 (2007), pp. 1369–1371. DOI: [10.1039/b616764k](https://doi.org/10.1039/b616764k).
- [12] Melis Özkan et al. "A [5]rotaxane-based photosensitizer for photodynamic therapy". In: *European Journal of Organic Chemistry* 2019.21 (2019), pp. 3534–3541. DOI: [10.1002/ejoc.201900278](https://doi.org/10.1002/ejoc.201900278).
- [13] Jonathan E. Buston, James R. Young, and Harry L. Anderson. "Rotaxane-encapsulated cyanine dyes: Enhanced fluorescence efficiency and photostability". In: *Chemical Communications* 11 (2000), pp. 905–906. DOI: [10.1039/b001812k](https://doi.org/10.1039/b001812k).
- [14] Min Feng et al. "Stable, Reproducible Nanorecording on Rotaxane Thin Films". In: *Journal of the American Chemical Society* 127.44 (2005). PMID: 16262375, pp. 15338–15339. DOI: [10.1021/ja054836j](https://doi.org/10.1021/ja054836j). eprint: <https://doi.org/10.1021/ja054836j>. URL: <https://doi.org/10.1021/ja054836j>.
- [15] J.-C. Olsen et al. "A neutral redox-switchable [2]rotaxane". In: *Org. Biomol. Chem.* 9 (20 2011), pp. 7126–7133. DOI: [10.1039/C10B05913K](https://doi.org/10.1039/C10B05913K). URL: <http://dx.doi.org/10.1039/C10B05913K>.
- [16] Victor Blanco et al. "A Switchable [2]Rotaxane Asymmetric Organocatalyst That Utilizes an Acyclic Chiral Secondary Amine". In: *Journal of the American Chemical Society* 136.13 (2014). PMID: 24649824, pp. 4905–4908. DOI: [10.1021/ja501561c](https://doi.org/10.1021/ja501561c). eprint: <https://doi.org/10.1021/ja501561c>. URL: <https://doi.org/10.1021/ja501561c>.
- [17] Dönüs Tuncel, Nesibe Cindir, and Ünsal Koldemir. "[5]rotaxane and [5]pseudorotaxane based on Cucurbit[6]Uril and anchored to a meso-tetraphenyl porphyrin". In: *Journal of Inclusion Phenomena and Macrocyclic Chemistry* 55.3-4 (2006), pp. 373–380. DOI: [10.1007/s10847-006-9112-3](https://doi.org/10.1007/s10847-006-9112-3).
- [18] Kai Liu et al. "Supramolecular Photosensitizers with Enhanced Antibacterial Efficiency". In: *Angewandte Chemie International Edition* 52.32 (2013), pp. 8285–8289. DOI: <https://doi.org/10.1002/anie.201303387>. eprint: <https://onlinelibrary.wiley.com/doi/pdf/10.1002/anie>.

201303387. URL: <https://onlinelibrary.wiley.com/doi/abs/10.1002/anie.201303387>.
- [19] Nicholas Pearce et al. "Selective photoinduced charge separation in perylenediimide-pillar[5]arene rotaxanes". In: *Nature Communications* 13.1 (2022). DOI: [10.1038/s41467-022-28022-3](https://doi.org/10.1038/s41467-022-28022-3).
- [20] Aisan Khaligh et al. "Photoactive Catalytically Self-Threaded 2D Polyrotaxane Network for Visible Light Activated Antimicrobial Phototherapy". In: *ACS Applied Polymer Materials* 2.12 (2020), pp. 5726–5734. DOI: [10.1021/acsapm.0c01010](https://doi.org/10.1021/acsapm.0c01010). eprint: <https://doi.org/10.1021/acsapm.0c01010>. URL: <https://doi.org/10.1021/acsapm.0c01010>.
- [21] Loup Verlet. "Computer "Experiments" on Classical Fluids. I. Thermodynamical Properties of Lennard-Jones Molecules". In: *Phys. Rev.* 159 (1 July 1967), pp. 98–103. DOI: [10.1103/PhysRev.159.98](https://doi.org/10.1103/PhysRev.159.98). URL: <https://link.aps.org/doi/10.1103/PhysRev.159.98>.
- [22] Herbert Goldstein. *Classical Mechanics*. Addison-Wesley, 1980.
- [23] J. E. Jones. "On the Determination of Molecular Fields. I. From the Variation of the Viscosity of a Gas with Temperature". In: *Proceedings of the Royal Society of London Series A* 106.738 (Oct. 1924), pp. 441–462. DOI: [10.1098/rspa.1924.0081](https://doi.org/10.1098/rspa.1924.0081).
- [24] J. E. Jones. "On the Determination of Molecular Fields. II. From the Equation of State of a Gas". In: *Proceedings of the Royal Society of London Series A* 106.738 (Oct. 1924), pp. 463–477. DOI: [10.1098/rspa.1924.0082](https://doi.org/10.1098/rspa.1924.0082).
- [25] E. T. Jaynes. "Gibbs vs Boltzmann Entropies". In: *American Journal of Physics* 33.5 (1965), pp. 391–398. DOI: [10.1119/1.1971557](https://doi.org/10.1119/1.1971557). eprint: <https://doi.org/10.1119/1.1971557>. URL: <https://doi.org/10.1119/1.1971557>.
- [26] C. E. Shannon. "A mathematical theory of communication". In: *The Bell System Technical Journal* 27.3 (1948), pp. 379–423. DOI: [10.1002/j.1538-7305.1948.tb01338.x](https://doi.org/10.1002/j.1538-7305.1948.tb01338.x).
- [27] José Weberszpil and Wen Chen. "Generalized Maxwell Relations in Thermodynamics with Metric Derivatives". In: *Entropy* 19 (Aug. 2017), p. 407. DOI: [10.3390/e19080407](https://doi.org/10.3390/e19080407).
- [28] Niels Hansen and Wilfred F. van Gunsteren. "Practical Aspects of Free-Energy Calculations: A Review". In: *Journal of Chemical Theory and Computation* 10.7 (2014). PMID: 26586503, pp. 2632–2647. DOI: [10.1021/ct500161f](https://doi.org/10.1021/ct500161f). eprint: <https://doi.org/10.1021/ct500161f>. URL: <https://doi.org/10.1021/ct500161f>.

- [29] Federico Fogolari, Alessandra Corazza, and Gennaro Esposito. “Free Energy, Enthalpy and Entropy from Implicit Solvent End-Point Simulations”. In: *Frontiers in Molecular Biosciences* 5 (2018). ISSN: 2296-889X. DOI: [10.3389/fmolb.2018.00011](https://doi.org/10.3389/fmolb.2018.00011). URL: <https://www.frontiersin.org/article/10.3389/fmolb.2018.00011>.
- [30] Yaşar Demirel and Vincent Gerbaud. “Chapter 1 - Fundamentals of Equilibrium Thermodynamics”. In: *Nonequilibrium Thermodynamics (Fourth Edition)*. Ed. by Yaşar Demirel and Vincent Gerbaud. Fourth Edition. Elsevier, 2019, pp. 1–85. ISBN: 978-0-444-64112-0. DOI: <https://doi.org/10.1016/B978-0-444-64112-0.00001-0>. URL: <https://www.sciencedirect.com/science/article/pii/B9780444641120000010>.
- [31] M A Moore. “Exactly Solved Models in Statistical Mechanics”. In: *Physics Bulletin* 34.4 (Apr. 1983), pp. 167–167. DOI: [10.1088/0031-9112/34/4/045](https://doi.org/10.1088/0031-9112/34/4/045). URL: <https://doi.org/10.1088/0031-9112/34/4/045>.
- [32] Robert F. Sekerka. “16 - Microcanonical Ensemble”. In: *Thermal Physics*. Ed. by Robert F. Sekerka. Amsterdam: Elsevier, 2015, pp. 257–276. ISBN: 978-0-12-803304-3. DOI: <https://doi.org/10.1016/B978-0-12-803304-3.00016-8>. URL: <https://www.sciencedirect.com/science/article/pii/B9780128033043000168>.
- [33] A. Satoh. “Chapter 2 - Statistical Ensembles”. In: *Introduction to Molecular-Microsimulation of Colloidal Dispersions*. Ed. by A. Satoh. Vol. 17. Studies in Interface Science. Elsevier, 2003, pp. 7–18. DOI: [https://doi.org/10.1016/S1383-7303\(03\)80030-3](https://doi.org/10.1016/S1383-7303(03)80030-3). URL: <https://www.sciencedirect.com/science/article/pii/S1383730303800303>.
- [34] Phil Attard. “On the density of volume states in the isobaric ensemble”. In: *The Journal of Chemical Physics* 103.22 (1995), pp. 9884–9885. DOI: [10.1063/1.469956](https://doi.org/10.1063/1.469956). eprint: <https://doi.org/10.1063/1.469956>. URL: <https://doi.org/10.1063/1.469956>.
- [35] Xiang Gao, Emilio Gallicchio, and Adrian E. Roitberg. “The generalized Boltzmann distribution is the only distribution in which the Gibbs-Shannon entropy equals the thermodynamic entropy”. In: *The Journal of Chemical Physics* 151.3 (2019), p. 034113. DOI: [10.1063/1.5111333](https://doi.org/10.1063/1.5111333). eprint: <https://doi.org/10.1063/1.5111333>. URL: <https://doi.org/10.1063/1.5111333>.
- [36] Sebastian Kmiecik et al. “Coarse-Grained Protein Models and Their Applications”. In: *Chemical Reviews* 116.14 (2016). PMID: 27333362, pp. 7898–7936. DOI: [10.1021/acs.chemrev.6b00163](https://doi.org/10.1021/acs.chemrev.6b00163). eprint: <https://doi.org/10.1021/acs.chemrev.6b00163>.

- 10.1021/acs.chemrev.6b00163. URL: <https://doi.org/10.1021/acs.chemrev.6b00163>.
- [37] Elena Papaleo. “Integrating atomistic molecular dynamics simulations, experiments, and network analysis to study protein dynamics: strength in unity”. In: *Frontiers in Molecular Biosciences* 2 (2015). ISSN: 2296-889X. DOI: 10.3389/fmolb.2015.00028. URL: <https://www.frontiersin.org/article/10.3389/fmolb.2015.00028>.
- [38] H. J. C. Berendsen et al. “Molecular dynamics with coupling to an external bath”. In: *The Journal of Chemical Physics* 81.8 (1984), pp. 3684–3690. DOI: 10.1063/1.448118. eprint: <https://doi.org/10.1063/1.448118>. URL: <https://doi.org/10.1063/1.448118>.
- [39] Giovanni Bussi, Davide Donadio, and Michele Parrinello. “Canonical sampling through velocity rescaling”. In: *The Journal of Chemical Physics* 126.1 (2007), p. 014101. DOI: 10.1063/1.2408420. eprint: <https://doi.org/10.1063/1.2408420>. URL: <https://doi.org/10.1063/1.2408420>.
- [40] M. Parrinello and A. Rahman. “Polymorphic transitions in single crystals: A new molecular dynamics method”. In: *Journal of Applied Physics* 52.12 (1981), pp. 7182–7190. DOI: 10.1063/1.328693. eprint: <https://doi.org/10.1063/1.328693>. URL: <https://doi.org/10.1063/1.328693>.
- [41] Szilárd Páll and Berk Hess. “A flexible algorithm for calculating pair interactions on SIMD architectures”. In: *Computer Physics Communications* 184.12 (2013), pp. 2641–2650. ISSN: 0010-4655. DOI: <https://doi.org/10.1016/j.cpc.2013.06.003>. URL: <https://www.sciencedirect.com/science/article/pii/S0010465513001975>.
- [42] Brad A. Wells and Alan L. Chaffee. “Ewald Summation for Molecular Simulations”. In: *Journal of Chemical Theory and Computation* 11.8 (2015). PMID: 26574452, pp. 3684–3695. DOI: 10.1021/acs.jctc.5b00093. eprint: <https://doi.org/10.1021/acs.jctc.5b00093>. URL: <https://doi.org/10.1021/acs.jctc.5b00093>.
- [43] T.R.S. Prasanna. “Physical meaning of the Ewald sum method”. In: *Philosophical Magazine Letters* 92.1 (Jan. 2012), pp. 29–37. DOI: 10.1080/09500839.2011.622725. URL: <https://doi.org/10.1080%2F09500839.2011.622725>.
- [44] Thomas A. Darden, Darrin M. York, and Lee G. Pedersen. “Particle mesh Ewald: An Nlog(N) method for Ewald sums in large systems”. In: *Journal of Chemical Physics* 98 (1993), pp. 10089–10092.

- [45] Frank Eisenhaber et al. "The Double Cubic Lattice Method: Efficient Approaches to Numerical Integration of Surface Area and Volume and to Dot Surface Contouring of Molecular Assemblies". In: *Journal of Computational Chemistry* 16 (Mar. 1995), pp. 273–284. DOI: [10.1002/jcc.540160303](https://doi.org/10.1002/jcc.540160303).
- [46] Vijay S. Pande, Alexei R. Khokhlov, Alexander Yu. Grosberg. *Statistical physics of macromolecules*. AIP Press. s. 2002.
- [47] Andrea Amadei, Antonius B. M. Linssen, and Herman J. C. Berendsen. "Essential dynamics of proteins". In: *Proteins: Structure, Function, and Bioinformatics* 17.4 (1993), pp. 412–425. DOI: <https://doi.org/10.1002/prot.340170408>. eprint: <https://onlinelibrary.wiley.com/doi/pdf/10.1002/prot.340170408>. URL: <https://onlinelibrary.wiley.com/doi/abs/10.1002/prot.340170408>.
- [48] Daniel Herschlag and Margaux M. Pinney. "Hydrogen Bonds: Simple after All?" In: *Biochemistry* 57.24 (2018). PMID: 29678112, pp. 3338–3352. DOI: [10.1021/acs.biochem.8b00217](https://doi.org/10.1021/acs.biochem.8b00217). eprint: <https://doi.org/10.1021/acs.biochem.8b00217>. URL: <https://doi.org/10.1021/acs.biochem.8b00217>.
- [49] A. Shrake and J.A. Rupley. "Environment and exposure to solvent of protein atoms. Lysozyme and insulin". In: *Journal of Molecular Biology* 79.2 (1973), pp. 351–371. ISSN: 0022-2836. DOI: [https://doi.org/10.1016/0022-2836\(73\)90011-9](https://doi.org/10.1016/0022-2836(73)90011-9). URL: <https://www.sciencedirect.com/science/article/pii/0022283673900119>.
- [50] Alpeshkumar K. Malde et al. "An Automated Force Field Topology Builder (ATB) and Repository: Version 1.0". In: *Journal of Chemical Theory and Computation* 7.12 (2011). PMID: 26598349, pp. 4026–4037. DOI: [10.1021/ct200196m](https://doi.org/10.1021/ct200196m). eprint: <https://doi.org/10.1021/ct200196m>. URL: <https://doi.org/10.1021/ct200196m>.
- [51] Bruno A. C. Horta et al. "A GROMOS-Compatible Force Field for Small Organic Molecules in the Condensed Phase: The 2016H66 Parameter Set". In: *Journal of Chemical Theory and Computation* 12.8 (2016). PMID: 27248705, pp. 3825–3850. DOI: [10.1021/acs.jctc.6b00187](https://doi.org/10.1021/acs.jctc.6b00187). eprint: <https://doi.org/10.1021/acs.jctc.6b00187>. URL: <https://doi.org/10.1021/acs.jctc.6b00187>.
- [52] Tomáš Raček et al. "Atomic charge calculator II: Web-based tool for the calculation of partial atomic charges". In: *Nucleic Acids Research* 48.W1 (2020). DOI: [10.1093/nar/gkaa367](https://doi.org/10.1093/nar/gkaa367).

- [53] Radka Varekova et al. "Electronegativity equalization method: Parameterization and validation for large sets of organic, organohalogen and organometal molecule". In: *International Journal of Molecular Sciences* 8.7 (2007), pp. 572–582. DOI: [10.3390/i8070572](https://doi.org/10.3390/i8070572).
- [54] Anthony K. Rappe and William A. Goddard. "Charge equilibration for molecular dynamics simulations". In: *The Journal of Physical Chemistry* 95.8 (1991), pp. 3358–3363. DOI: [10.1021/j100161a070](https://doi.org/10.1021/j100161a070). eprint: <https://doi.org/10.1021/j100161a070>. URL: <https://doi.org/10.1021/j100161a070>.
- [55] Elizabeth Durham et al. "Solvent accessible surface area approximations for rapid and accurate protein structure prediction". In: *Journal of Molecular Modeling* 15.9 (2009), pp. 1093–1108. DOI: [10.1007/s00894-009-0454-9](https://doi.org/10.1007/s00894-009-0454-9).
- [56] Thomas F. Willems et al. "Algorithms and tools for high-throughput geometry-based analysis of crystalline porous materials". In: *Microporous and Mesoporous Materials* 149.1 (2012), pp. 134–141. ISSN: 1387-1811. DOI: <https://doi.org/10.1016/j.micromeso.2011.08.020>. URL: <https://www.sciencedirect.com/science/article/pii/S1387181111003738>.